Submitted to Astrophysical Journal 6/14/02, Revised 12/13/02

BOOMERANG : A Balloon-borne Millimeter Wave Telescope and Total Power Receiver for Mapping Anisotropy in the Cosmic Microwave Background

B.P. Crill[1,2], P.A.R. Ade[3], D. R. Artusa[1], R.S. Bhatia[1], J.J. Bock[1,4], A. Boscaleri[5], P. Cardoni[6], S. E. Church[7], K. Coble[8,9], P. deBernardis[10], G. deTroia[10], P. Farese[11], K. M. Ganga[12], M. Giacometti[7], C. V. Haynes[13], E. Hivon[1,12], V.V. Hristov[1], A. Iacoangeli[6], W.C. Jones[1],A.E. Lange[1], L. Martinis[7], S. Masi[10], P.V. Mason[1,4],P.D. Mauskopf[3], L. Miglio[14], T. Montroy[11], C.B. Netterfield[14], C. G. Paine[1,4], E. Pascale[5], F. Piacentini[10], G. Polenta[9], F. Pongetti[15], G. Romeo[15], J.E. Ruhl[16], F. Scaramuzzi[7], D. Sforna[6], and A.D. Turner[4].

[1] *Observational Cosmology, MS 59-33, California Institute of Technology, Pasadena, CA 91125, USA*

[2] *Physics Department, California State University - Dominguez Hills, Carson, CA 90747, USA (Current Affilliation)*

[3] *Department of Physics and Astronomy, Cardiff University, Cardiff CF24 3YB, UK*

[4] *Jet Propulsion Laboratory, Pasadena, CA, USA*

[5] *IROE-CNR, Firenze, Italy*

[6] *ENEA, Frascati, Italy*

[7] *Department of Physics, Stanford Univ., Palo Alto, CA, USA*

[8] *University of Chicago Dept. of Astronomy and Astrophysics, Chicago, IL, USA*

[9] *Adler Planetarium and Astronomy Museum, Chicago, IL, USA*

[10] *Dipartimento di Fisica, Universitá La Sapienza, Roma, Italy*

[11] *Department of Physics, Univ. of California, Santa Barbara, CA, USA*

[12] *Infrared Processing and Analysis Center, Pasadena, CA, USA*

[13] *Queen Mary and Westfield College, London, UK*

[14] *Department of Astronomy, University of Toronto, 60 George St, Toronto ON M5S 3H8, Canada*

[15] *Istituto Nazionale di Geofisica, Roma, Italy*

[16] *Physics Department, Case Western Reserve University, Cleveland, OH, USA*

ABSTRACT

We describe BOOMERANG; a balloon-borne microwave telescope designed to map the Cosmic Microwave Background (CMB) at a resolution of $10'$ from

the Long Duration Balloon (LDB) platform. The millimeter-wave receiver employs new technology in bolometers, readout electronics, cold re-imaging optics, millimeter-wave filters, and cryogenics to obtain high sensitivity to CMB anisotropy. Sixteen detectors observe in 4 spectral bands centered at 90, 150, 240 and 410 GHz. The wide frequency coverage, the long duration flight, the optical design and the observing strategy provide strong rejection of systematic effects. We report the flight performance of the instrument during a 10.5 day stratospheric balloon flight launched from McMurdo Station, Antarctica that mapped $\sim$ 2000 square degrees of the sky.

Subject headings: cosmology: cosmic microwave background, anisotropy, measurements, power spectrum, instrumentation

1. Introduction

Measurements of the angular power spectrum of anisotropy in the Cosmic Microwave Background (CMB) are greatly enhancing our knowledge of fundamental properties of the universe. In particular, models of the early universe predict the existence of a series of harmonic peaks in the angular power spectrum at degree scales. The precise determination of the amplitude and angular scale of the peaks provides strong constraints on these models and enables their parameters to be determined with great precision (Sachs and Wolfe (1967); Hu et al. (1997)). After the discovery of the large scale anisotropies by COBE-DMR (Bennett et al. (1996)), a host of ground-based and balloon-borne observations detected a first peak at a multipole moment of $\ell \sim 200$ in the angular power spectrum of the CMB (Bond, Jaffe and Knox (2000);Miller et al. (1999);Mauskopf et al. (2000)). Here we describe the BOOMERANG experiment, which has made a deep map of the CMB at sub-degree resolution and a precision measurement of the angular scale and amplitude of the first peak (de Bernardis et al. (2000); de Bernardis et al. (2002)) from the Long Duration Balloon (LDB) platform.

The BOOMERANG instrument consists of a 1.3-m off-axis telescope that feeds a bolometric array receiver. The receiver is housed inside a long duration liquid helium cryostat. A sorption pumped ^{3}He refrigerator maintains the detectors at 280 mK. Observations are made in 4 spectral bands centered at 90, 150, 240, and 410 GHz (3mm, 2mm, 1.3mm, and 750 μm) with angular resolutions of $18'$, $10'$, $14'$, and $13'$ FWHM respectively. A test flight of the BOOMERANG payload in a different configuration (Piacentini et al. (2002)) flew in a 6 hour engineering flight from Palestine, Texas in 1997 (Mauskopf et al. (2000); Melchiorri et al. (1999)). The configuration of the instrument described here flew in a 252 hour flight from McMurdo Station, Antarctica in 1998-1999.

2. Instrument Overview

BOOMERANG incorporates four unique design features that allow a precision measurement of the angular power spectrum of the CMB. First, BOOMERANG is a quasi total-power radiometer. The temperature of one part of the sky is measured relative to its surroundings by slowly (scan period 1-2 minutes) scanning the entire telescope in azimuth. The output from each detector is AC coupled to an amplifier. The scan appears at very low frequency (0.008 - 0.016 Hz). The stable, virtually transparent atmosphere at balloon float altitude and the intrinsic stability of the bolometric detectors and readout amplifier chain make it possible to map large areas of the sky with high sensitivity.

Second, BOOMERANG is designed to take advantage of the long integration time possible from a balloon borne platform flown over the Antarctic. During the austral summer, the polar vortex winds provide a stable orbit for balloons at the top of the stratosphere ($\sim$ 38 km altitude) at a distance of 1200 km from the pole. This observation platform provides flight durations of 7 to 20 days, thus allowing measurements to be repeated many times in order to check for systematic effects. The relatively small fraction (<10%) of the sky that is accessible from a balloon platform during the austral summer fortuitously includes the part of the sky that is lowest in foreground contamination (Schlegel et al. (1998)).

Third, the BOOMERANG receiver has a high instantaneous sensitivity, due to its optimized low-background bolometers and high-bandwidth feeds operating at cryogenic temperatures. The channels at 90 GHz and 150 GHz are positioned in frequency to optimally avoid galactic foreground contamination. Combining these channels with those at 240 GHz and 410 GHz allows powerful detection and removal of foreground signals.

Finally, the BOOMERANG receiver uses re-imaging optics that provide excellent image quality over a large focal plane. The receiver simultaneously measures 16 bolometer channels in 8 pixels with beams separated by up to 4° on the sky. The wide format of the focal plane and large number of detectors allowed by the re-imaging optics provides the ability to detect and remove temporally correlated noise, since observations of a specific region of the sky by different detectors are well-separated in time.

3. Instrument Description

3.1. Detectors

BOOMERANG uses silicon nitride micromesh "spider web" bolometers (Bock et al. (1996)) that were developed specifically for use in an environment with a high cosmic ray flux,

such as above the Earth's polar regions. The bolometer consists of a finely photolithographed mesh that provides high absorption efficiency over a wide band with low heat capacity and cosmic ray cross section (Figure 1). A Neutron Transmutation Doped (NTD) germanium thermistor provides high sensitivity and extremely good stability. The fundamental limit of the sensitivity of a bolometer is phonon noise in the thermal link between the absorber and the heat sink. In this case the Noise Equivalent Power, $NEP = \gamma\sqrt{4k_BT^2G}$ where G is the thermal conductance, T is the bath temperature, and $\gamma \sim 1.2$ takes into account the contribution from Johnson noise in the NTD Ge thermistor. For a given background load Q, maximum sensitivity is achieved for $G \sim Q/T$ (Mather (1984)). The desired time constant of a bolometer $\tau \sim C/G$ (where C is the heat capacity of the bolometer) for a given modulation scheme sets a limit on the minimum thermal conductance that can be selected. The bolometers are optimized for a 10 K Rayleigh-Jeans spectrum background (Grannan et al. (1997)).

3.2. Readout Electronics

The slow scan observation scheme requires stability of the detector and the readout electronics, from the bolometer thermal cutoff frequency ($\sim$ 10 Hz) down to the characteristic scan frequency at tens of mHz. The detector readout scheme implements an electronic modulation/demodulation technique to provide stability at low frequency, by moving the signal bandwidth well above the 1/f knee of the JFET and the warm amplifer. Modulation is achieved by biasing the bolometer with an AC current.

The detectors are AC voltage biased with a 318 Hz sine wave. Dual 10MΩ load resistors provide an approximate current bias. The signal from each detector passes through a JFET source follower circuit on the 2 K stage, lowering the output impedance and reducing the susceptibility to microphonics. The JFETs were selected for low power dissipation and are packaged by IR Labs (IR Labs TIA).

The signal from the cold JFETs passes through a preamplifier stage and a band pass filter stage prior to reaching the synchronous detector.

The synchronous demodulator (lock-in) multiplies the signal synchronously by +1/-1 times the bias reference. A 4-pole Butterworth low pass filter with cutoff at 20 Hz removes the high-frequency terms of the product and acts as an anti-aliasing filter for the Data Acquisition System (DAS). An AC-coupling high pass filter with a cutoff at 0.016 Hz and extra gain is applied to the signal to match the signal dynamics to the DAS dynamic range. The total gain of the amplifier chain is 5×10^4.

The entire readout electronics contribute less than 10 $nV_{rms}/\sqrt{Hz}$ to the signal noise in the frequency range of 0.016 Hz to 20 Hz. The AC-coupled signals are sampled by the DAS at 60 Hz. Figure 2 shows a block diagram of the analog readout electronics.

The DAS is constructed entirely from discrete CMOS logic, with the data frame defined by a UV-EPROM. The 38 kbps bi-phase output is sent to a line-of-sight transmitter and to the data storage system. The data stream is also stored on board by a pair of redundant commercial grade 486DX/4 PC's to commercial hard disks and to a Digital Audio Tape (DAT). The PC's additionally compress the data and send it over a 4 kilobit s^{-1} TDRSS satellite link to the ground station for in-flight viewing. The PC's are housed in a pressure vessel to maintain 1 atmosphere of pressure for the hard disks.

3.3. Rejection of RF and Microphonic Interference

Bolometric detectors are susceptible to spurious heating from radio frequency interference (RFI) dissipated in the thermistor or to pickup from microphonic response of the bolometer or wiring. This is especially of concern at the high impedance portion of the wiring between the bolometer and the cold JFET followers. There are several microwave transmitters for satellite communcations on board the BOOMERANG payload that are potentially sources of RF pickup in the bolometers. The frequencies of concern are an ARGOS 400 MHz transmitter and a TDRSS 2.3 GHz transmitter.

To keep RFI power from reaching the detectors, each bolometer cavity is constructed as a Faraday cage. The only entrances into this cage are through the feed horn and via the wiring to the detector. The feed horn has a waveguide cutoff at the lower edge of the band, preventing any RFI from reaching the detector via that path. The wires that exit the cavity are connected to ground through surface mount 20 pF capacitors that provide protection from RFI close to the detector. All bolometer leads from the JFET preamp stage to the warm amplifiers run through cast eccosorb filters. The cast eccosorb filters consist of stripline cables potted in cast eccosorb (EV Roberts CR-124) and have significant attenuation above a few GHz. These provide the only exit from a second Faraday cage surrounding the 2 K stage.

A third Faraday cage surrounds the bolometers, room temperature amplifers, cryostat electronics and wiring. The amplified signals exit the third Faraday cage through Spectrum II filters (Spectrum 1212-0502) to the DAS.

The low suspended mass of the micromesh bolometers naturally provides a reduction in microphonic response (measured resonant frequency >1 kHz). The high impedance wiring

connecting the bolometers to the JFET follower stage is carefully tied down. The wiring on the 0.3 K stage consists of 27 AWG shielded twisted pair that is strapped down with teflon tape and nylon cord. Between the 0.3 K and 2 K stages, cables made with low thermal conductivity 50 μm manganin wire are strapped to the Vespel posts that support the cold stage. Inside the JFET box, all high impedance wires are potted in silicone RTV.

3.4. Cryostat

The cryogenic system for BOOMERANG keeps the detectors at their operating temperature of 0.28 K for the entire two weeks of an LDB balloon flight. It has 60 liters of volume at 2 K to contain the photometers, re-imaging optics, baffles, and cold preamplifiers. The system is composed of a self contained sorption-pumped ^{3}He refrigerator (Masi et al. (1998)) and a helium/nitrogen main cryostat (Masi et al. (1999)). The ^{3}He fridge contains 34 liters STP of ^{3}He and runs at 0.280 K with a load of 27 μW. The main cryostat holds 65 liters of liquid nitrogen and 69 liters of liquid helium. The tanks, toroidal in shape, are suspended by Kevlar cords. Radiation from 300 K to the 77 K tank is shielded by a blanket of 30 layers of aluminized mylar superinsulation. Radiation from the 77 K tank to the helium tank is shielded by an intermediate temperature shield cooled to < 20 K by the boiloff from the helium tank. External plumbing with electrically actuated valves is used to pressurize the nitrogen bath during the flight and to maintain the low pressure of the helium bath during ascent. The helium bath is vented to ambient pressure at float altitude to maintain the lowest possible temperature.

3.5. Optics

The BOOMERANG telescope (Figure 3) consists of an ambient temperature (-20° C in the shade at float altitude) off-axis parabolic primary mirror that feeds a pair of cold re-imaging mirrors inside the cryostat. The primary mirror is 1.3 m in diameter and has a 45° off-axis angle for a projected size of 1.3×1.2 m. The mirror and receiver can be tipped in elevation by $+10°$ and $-12°$ to cover elevation angles from 33° to 55°. Radiation from the sky is reflected by the primary mirror and passes into the cryostat through a thin (50 μm) polypropylene vacuum window near the prime focus. The window is divided in two circles side by side, each 6.6 cm in diameter. Filters to reject high frequency radiation and to reduce the thermal load on the 2 K and 0.3 K stages of the cryostat are mounted on the 77 K and 2 K shields in front of the cold mirrors. These are capacitive multilayer metal mesh low pass filters with cutoffs at 540 GHz and 480 GHz respectively. Neutral density filters

with transmission of 1.5% used to reduce the loading on the detectors for ground testing are mounted on a mechanism that can move the filters in and out of the beam near the prime focus.

Off-axis ellipsoidal secondary and tertiary mirrors surrounded by black baffles re-image the prime focus onto a detector focal plane with diffraction-limited performance at 1 mm over a $2^\circ \times 5^\circ$ field of view.

The re-imaging optics form an image of the primary mirror at the 10 cm diameter tertiary mirror. The size of the tertiary mirror limits the geometric illumination of the primary mirror to the central 50% in area to reduce sidelobe response.

The secondary and tertiary mirrors are ellipsoidal reflectors with effective focal lengths of 20 cm and 33 cm respectively. The mirrors have been optimized with CodeV software (Mauskopf (1996)). The prime focus is fed from the illuminated portion of the primary at f/2, so the detector focal plane is fed at f/3.3. The tertiary mirror is 10 cm in diameter, corresponding to an 85 cm diameter aperture on the 1.3 m diameter primary.

The BOOMERANG focal plane contains four single-frequency channels fed by smooth-walled conical horns and four multicolor photometers fed by parabolic concentrators (Winston horns). Although the image quality from the optics is diffraction limited at 150 GHz over a $2^\circ \times 5^\circ$ field, all of the feed optics are placed inside two circles 2° in diameter, separated center to center by 3.5°. The focal plane area outside these circles is unusable because it is vignetted by blocking filters at the entrance to the 2 K optics box and on the 77 K shield. The horn positions are optimized using geometric ray tracing. All of the feeds are oriented towards the center of the tertiary mirror. The phase center of the conical horns and the center of the aperture of the parabolic horns are placed at the focus.

A schematic of the relative positions and sizes of the beams on the sky is shown in Figure 4. The focal plane layout is chosen so as to repeat observations of the same part of the sky on many different time scales. The telescope scans in azimuth, and at 1 degree per second (dps) at 45° elevation, channels on opposite sides of the focal plane will observe the same sky ~ 2 s apart. The rotation of the sky above Antarctica allows each row of detectors to observe the same patch of sky ~ 30 minutes apart.

3.6. Focal Plane

3.6.1. Single-mode photometers

The focal plane contains four single-frequency channels; two at 90 GHz and two at 150 GHz (Figure 5). The feeds are similar to those that will be used on the Planck Surveyor HFI (Church et al. (1996)). The dual-polarization feed structures are designed to provide low thermal load on the 0.3 K stage, high efficiency and excellent control of frequency and spatial response within a compact structure.

The entrance feeds are smooth-walled conical feeds designed to illuminate the tertiary mirror with a -5 dB edge taper. Using Gaussian optics, the desired edge taper defines the beam waist at the phase center of the horn, that in turn defines a relation between the horn aperture diameter and the horn length. The solution with minimum length is selected, which gives diameters of 19.66 mm and 11.8 mm and flare angles of 19.7° and 10.5° for the 90 GHz and 150 GHz structures respectively.

At the throat of the entrance feed, a 2λ length of waveguide with a radius $r = 0.35\lambda$ defines the low frequency edge of the passband and sets the throughput of the feed structure such that only the lowest order Gaussian mode is propagated through the rest of the system. For the 90 and 150 GHz structures, 2.54 mm and 1.33 mm diameter guides define cutoffs at 69 GHz and 132 GHz respectively.

An f/4 re-expanding horn re-emits the light through band defining filters and into an identical reconcentrating horn that feeds the light into the detector cavity. Identical low density polyethylene hyperbolic lenses are placed at the aperture of each of the two face-to-face horns to improve the coupling. The focal length of the lenses is set to maximally match the lowest order Gaussian mode propagating from each horn through the intervening filters in the thin lens approximation.

The filter stack consists of two capacitive metal mesh filters (Timusk and Richards (1981), Lee et al. (1996)) and an alkali-halide/carbon layered polyethylene filter(Yamada et al. (1962)). The first capacitive metal mesh filter defines the upper edge of the band while the second is tuned to a higher cutoff frequency and is used to block leaks in the first filter. In the 150GHz feeds, filters with cutoffs at 168 and 198 GHz are used, while in the 90 GHz feeds, 99 and 177 GHz filters are used. The alkali-halide/carbon layered polyethylene filter blocks infrared and optical light ($\nu > 1650$ GHz) and is tuned in thickness to maximize transmission at the center of the feed.

Each detector is mounted in an integrating cavity a distance $\lambda/4$ from the exit aperture of the re-concentrating horn and at a distance $\lambda/4$ from a backshort in order to maximize

the electric field at the absorber (Glenn et al. (2002)).

We use foam eccosorb thermal loads at 300 K and at 77 K to measure the optical efficiency of each of the feed structures. The difference in optical power is measured by comparing the I vs. V load curves of the bolometer under the two different background conditions. We measure optical efficiencies of 28% for the 150 GHz feed structure and 43% for the 90 GHz feed.

3.6.2. Multi-color photometers

The focal plane for the Antarctic LDB flight of BOOMERANG contains 4 three-color photometers (Figure 6) similar to those used in the FIRP instrument on IRTS (Lange et al. (1994)), MAX (Fischer et al. (1992)), and SuZIE (Mauskopf et al. (2001)). These structures have the advantage of simultaneous observation of the same region of sky in three frequency bands.

Back to back parabolic concentrators (Welford and Winston (1989)) mounted on the 2 K stage feed the photometers. The input horn is set at f/3.4 to maximally couple to the re-imaging optics. The horn has an entrance aperture diameter of 1 cm producing a $12'$ beam on the sky, corresponding to the diffraction limit at 150 GHz. The entrance aperture of the horn has a short flare in the shape of a 45° section of a circle with a diameter of 1.3 cm to reduce sidelobes at low frequency.

The throughput of the photometer is defined to be 0.05 cm^2 sr by the 1.45 mm diameter exit aperture of the parabolic horn. The re-expanding parabolic horn has an aperture that matches a light pipe located on the 0.3 K stage across a 0.5 mm gap. At the entrance to the light pipe, there is a metal mesh low pass filter with a cutoff of 480 GHz to improve the out-of-band rejection.

In the light pipe, two dichroic filters tipped 22.5° off-axis direct light at frequencies greater than 270 GHz and 180 GHz through inductive multilayer metal mesh bandpass filters that pass 410 GHz and 240 GHz respectively. Radiation at frequency less than 180 GHz is transmitted through the two dichroics and through a 150 GHz bandpass filter. Parabolic horns concentrate the light into integrating bolometer cavities where it is detected.

The three bolometers simultaneously observe the same part of the sky; however the beam patterns of the three channels are quite different. At 150 GHz, the entrance feed is single-moded, and by 410 GHz the system is close to the geometrical optics limit. The 150 GHz beam is well-described by a Gaussian, and the 410 GHz the beam is close to a top-hat.

At 240 GHz, several modes propagate in the horn, and the beam contains a mode which is annular in shape.

3.6.3. Spectral Bandpass

The spectral bandpass of the instrument is measured pre-flight using a Fourier transform spectrometer (FTS). Interferograms are measured for each channel and Fourier transformed to measure the spectral response. The final spectra are corrected for the 250 μm thick polypropylene beam splitter and the spectrum of the 77K thermal source. The bandpasses are plotted in figure 7.

Blocking each band with a high pass filter (thick grill filter) with a cut-off frequency just above the band allows a search for leaks at high frequency. Since this test is sensitive to integrated leaks, a much higher signal to noise measurement can be made than with the FTS. The signals produced by a chopped LN_2 source viewed with and without a thick grill high pass filter in the beam were compared. Table 1 lists the results.

3.7. Calibration Lamp

A 1 cm diameter hole located in the center of the tertiary mirror contains a micromesh bolometer with copper leads for use as a calibration lamp. A germanium thermistor provides high impedance at 2 K. The electronics send a 1 second pulse of current through the thermistor every 13 minutes, heating the bolometer and providing an optical pulse to be used as a transfer calibrator.

3.8. Attitude Control System

The telescope is designed to smoothly scan in azimuth while at fixed elevation, and has an attitude control system similar to those described in Boscaleri et al. (1990a), Boscaleri et al. (1990b), and Boscaleri et al. (1994). The azimuth pointing of the telescope is controlled by two torque motors (Inland QT6205d); the first spins a large flywheel; the other torques against the flight train of the balloon. The two motors provide enough torque to move the gondola in azimuth and to correct for random rotation of the balloon.

The elevation can be controlled by tipping the inner frame of the telescope with a ball screw linear actuator (SKF CARN-32-300-1) driven by a DC gearmotor (QT-1209-B).

Payload pendulations were reduced by an oil-filled damper mounted near the flight train. An overview of the gondola frame is shown in Figure 8. The fully digital control hardware consists of two redundant 386 CPU's. A watchdog circuit switches control of the pointing from one CPU in a few hundred milliseconds in case of reboot.

Pointing information is provided by a differential GPS array, a two-axis sun sensor (Romeo et al. (2002)), an encoder on the elevation axis, and three orthogonal axis laser rate gyroscopes. The azimuth gyroscope provides velocity feedback for controlling the scan of the telescope. The absolute pointing data from the sun sensor is used to reset the drift in the gyroscopes and to provide data for post-flight attitude reconstruction

The telescope is powered by two solar power systems with lead-acid battery backup. The cryostat, receiver, and DAS are on a 300W system and the attitude control system and data storage are on a second system with a 750W maximum.

3.9. Thermal Design

The outside of the gondola is paneled with 50 μm mylar bonded to 25 μm thick aluminum foil. With the mylar side facing outwards, the combination of layers provides high reflectivity in the optical band and high emissivity in the infrared band, thus protecting the payload from excessive solar heating.

A thermal model is constructed for the payload that included heat transfer by conduction and radiation alone. Two cases were considered for the input power: "cold" and "hot". The cold case assumed that the payload would drift over water and receive 1044 W m^{-2} radiation from the sun and a 9% albedo for the surface of the earth for 177 W m^{-2} of power. The hot case assumed that the payload would be above fresh snow and receive 1397 W m^{-2} radiation from the sun and 213 W m^{-2} from the earth with an albedo of 95%. Table 2 shows the predicted range of ambient temperatures.

4. Observations

BOOMERANG was launched from Williams Field at McMurdo Station (Antarctica) on December 29, 1998 at 3:30 GMT on a 27 million cubic foot balloon with tied ducts and no radar tape. The payload launch weight was 1600 kg including 70 kg of glass ballast. The instrument reached float altitude (38km) three hours later and began observations immediately. The telescope remained within 1.5° of $\sim$ 78° S latitude as it circumnavigated the continent. The flight lasted 259 hours and was terminated 50 km south of the launch site.

The majority of the flight was spent in CMB observation mode, that consisted of scanning the telescope in a smoothed triangle wave with a 60° peak- to-peak amplitude in azimuth at fixed elevation. The center of the scan was set so that the region of sky away from the galactic plane was mapped within the constraint of sun-avoidance. As the earth rotated, the scan center and scan direction on the celestial sphere changed. At a single elevation, one day of scanning provided a coverage of 22° in declination and gave scans tipped at ±11°, providing cross-linking of the scans (Figure 9).

Two scan speeds were used in CMB mode; 1 degree per second (dps) and 2 dps. The elevation of the telescope was changed roughly daily between angles of 40°, 45°, and 50°. Every 90 minutes, a 120° peak-to-peak scan centered on the anti-sun direction was conducted for 5 minutes as a check for systematic effects due to the sun. Several HII regions in the galactic plane were targeted during the flight as potential cross-calibrators and beam mapping sources. These were RCW38, RCW57 (a double source composed of NGC3603 and NGC3576), IRAS/08576, IRAS/1022, and the Carina Nebula. Three known clusters (A3158, A3112, A3226) were targeted in a search for the Sunyaev-Zel'dovich effect. Three extragalactic point sources were observed serendipitously in the CMB map: the blazar 0537–441 (8544), the BL Lac 0521–365 (8036), and the QSO 0438–443 (7044). Table 3 shows the total time spent in each scan mode.

5. Flight Performance

5.1. Detector System

5.1.1. Transfer Function

A cosmic ray hit on a bolometer is well approximated by a delta function power input, and can be used to measure the transfer function of the bolometer and electronics. The transfer function of the experiment is parameterized by the thermal time constant of the bolometer and the properties of the anti-aliasing filters and AC-coupling in the readout electronics. The AC-coupling and anti-aliasing time constants are measured on the ground and are expected to be the same in flight since the electronics operating temperature in-flight is similar to that on the ground. However, the bolometer time constant is highly sensitive to the background optical load.

The combination of the theoretical transfer function of the bolometer (a single pole low pass filter) and the measured electronics transfer function is used to obtain the impulse response function.

A database of cosmic ray hits is built for each channel, simultaneously fitting an amplitude and phase shift to each hit as well as fitting the data to the impulse response function. Figure 10 shows the best fit template and the cosmic ray data for one of the 150 GHz channels. The best fit bolometer time constants for each channel are listed in Table 5.

The cosmic ray method is precise in the measure of the high frequencies in the transfer function. The low frequency side of the function is dominated by the 0.016 Hz AC-coupling filter. The best confirmation of the stability of the high pass time constants is made by the agreement of the calibration on the CMB dipole at the two scan speeds (Section 6 below).

5.1.2. Deglitching

The BOOMERANG bolometer data are contaminated with transient events that must be flagged and removed; these include cosmic ray hits, thermal events in the 0.3 K stage, calibration lamp signals, and short periods of electromagnetic interference (EMI).

Large thermal events in the 0.3 K stage and calibration signals appear simultaneously in all channels and are easily flagged. Smaller thermal relaxation events were found with a pattern matching algorithm. Cosmic ray hits, EMI spikes, and smaller thermal events occurring within an individual bolometer are found using two algorithms. First large spikes are detected as deviations of greater than 3σ in a three point difference function of the time ordered data, defined by $\delta_i = d_i - 0.5(d_{i-2} + d_{i+2})$, where d is the time-ordered sample and σ refers to the standard deviation of the data. Smaller glitches are found using an iterative binning scheme; the time stream data are binned into pixels on the sky and individual samples more than 4σ from the average value of a pixel are flagged and not used in the next iteration. After 4 iterations, a negligible number of new glitches are found.

The flagged data, identified by the methods given above, are replaced by a constrained realization of the noise and not used in subsequent analysis. Approximately 5% of the data in each channel are contaminated and flagged. Drifts in the bolometer data after large cosmic ray hits are removed by fitting a parabola to the data. Drifts induced by large thermal events are fit to an exponential and removed. These data are used in the subsequent analysis.

The average time between detected cosmic ray hits in each bolometer is 43 seconds.

5.1.3. Detector Noise

The voltage noise is determined by taking the power spectrum of the deglitched time domain data. It is then deconvolved with the detector and electronic transfer functions and converted to Noise Equivalent Temperature (NET) by dividing by the DC detector responsivity. Figure 11 shows the NET as a function of frequency of a 150 GHz channel and Table 5 shows the average NET of other detector channels.

During the 1 dps scans at 45° elevation, a signal on the sky with spherical multipole moment of $\ell = 200$ is mapped to a frequency of 0.38 Hz, well above the 1/f knee of the detector system.

5.2. Cryogenics

The cryogenic system performed well, keeping the detectors well below their required operating temperature of 0.3 K for the entire flight. Figure 12 shows cryogenic temperatures recorded during the 10.5 day flight. The daily oscillation of the main helium bath temperature is due to daily fluctuations of the external pressure. The altitude of the payload varies with the elevation of the sun, which oscillates between 11° to 35° diurnally.

We have searched for scan synchronous temperature fluctuations in the ^{3}He evaporator and in the ^{4}He temperature, and we find upper limits of the order of 1 μK_{rms} in the 1 dps scans, and drifts in the ^{3}He evaporator temperature with an amplitude of a few μK during the 2 dps scans (Figure 13). These temperature fluctations are likely related to the scan-synchronous noise observed during the 2 dps scans.

5.3. Payload

5.3.1. Electronic and Thermal Performance

The high cosmic ray flux above the Antarctic is a concern for digital electronics. Each of the two 486DX/4 based data storage system computers experienced two watchdog-induced reboots during the 259 hour flight. The reboots were not concurrent, so a continuous final data stream is reconstructed from the two systems. The discrete CMOS based Data Acquisition System and the 80386 PC based Attitude Control System experienced no in-flight lockups.

See Table 2 for a comparison of predicted temperatures with actual achieved tempera-

tures. The in-flight temperatures of the electronics were roughly 20°C warmer than predicted, perhaps due to white nylon blankets (not included in the model) placed over some of the electronics to avoid excessive cooling during ascent.

5.4. Optics

5.4.1. In-flight Detector Background

On day 8 of the flight, a partial I-V curve of each detector was measured. The bias voltage was commanded to 4 discrete levels. The optical power incident on the detector is determined by extrapolating the in-flight I vs. V load curve to zero electrical power. Using knowledge of the optical efficiency and the spectral bandpass, an average equivalent Rayleigh-Jeans temperature of 10 K was found. The precision of the background measurement is limited to $\sim 50\%$ by uncertainty in the knowledge of the resistance as a function of temperature of the NTD germanium thermistors.

5.4.2. Beam Shape

The intrinsic point spread function of each receiver is determined by the combined effect of the telescope, the feed, the feed's location in the focal plane, the spectral bandpass, the spectrum of the source, and the distance to the source. In addition there is a contribution to the effective beam on the sky associated with error in the pointing reconstruction. To first order, this pointing jitter manifests itself as an isotropic gaussian contribution to the beam size.

In order to determine the physical beam, the optical system is modeled with the ZEMAX ray tracing package (Focus Software, Inc.) as well as a physical optics code written specifically for BOOMERANG (Figure 14). The results of the models are verified with near field beam maps made with an ambient temperature eccosorb target. The eccosorb target has a Rayleigh-Jeans spectrum and allows a measurement of the beam down the the $\sim$ -20 dB level (Figure 15). To measure the far field radiation pattern on the sky, single cuts through bright HII regions (primarily RCW38) are made during pointed observations of the Galactic plane.

Due to the extended nature of the Galactic sources it is necessary to deconvolve the measured beam with the physical size of the source in order to recover the far field radiation pattern. Furthermore these sources do not exhibit the same spectrum as the CMB anisotropy

– the Galactic sources observed by BOOMERANG exhibit a sharply rising spectrum consistent with a combination of free-free emission and thermal emission from dust (Coble et al. (2002)). Nevertheless, scanned observations of bright HII regions near the Galactic plane are used to estimate the beam full width half maximum (FWHM) for each channel. These values are presented in Table 4 and Figure 16.

While the channels utilizing conical feed horns compare well with the beam map data, a $\sim 10\%$ discrepancy is observed between the calculated and measured FWHM of the photometer beams. In all cases, the measured FWHM are larger than the calculated beam size. This discrepancy is attributed to the multi–moded nature of the Winston concentrators utilized by these channels. For these channels the physical optics FWHM are scaled to fit the measurements of RCW38.

While these observations provide good statistics on the width of the main lobe, the dynamic range of the measurements are not sufficient to fully characterize the near sidelobe response and deviation from gaussianity of the beam. To obtain a detailed model of the near sidelobe response of the telescope, the physical optics calculation of the beam shape is performed for each channel using the measured position of the horns in the focal plane. The two dimensional far-field radiation patterns from the physical optics calculation scaled to fit the observed FWHM are then used to generate the window functions for each channel.

Observations of the position of the centroids of Galactic point sources provide a reliable way to quantify the contribution of the pointing uncertainty to the effective beam size for CMB observations. The scatter in the centroids of these objects in maps produced with the final version of the pointing reconstruction (Section 5.5) indicate that there is a pointing uncertainty of $2.5'$ (1σ).

The final beam model used for CMB analysis consists of the ZEMAX calculated beam (confirmed by the ground-based measurements) smeared with the measured pointing jitter.

The far sidelobes in the 150 GHz channels were measured before flight with a 150 GHz Gunn oscillator (Figure 17). Signal is rejected at all angles greater than $\sim 5^\circ$ at a level of $<$-55 dB. An upper limit to response from sources directly behind the telescope (eg the Sun) is set at $<$-82 dB.

5.5. Attitude Reconstruction

The attitude reconstruction is based on three sensors: the azimuth sun sensor, a three axis rate gyro, and a differential GPS. The conversion from Azimuth-Elevation to Right

Ascension-Declination additionally uses the time and position from a GPS receiver.

The azimuth sun sensor provides a precise ($< 1'$) and repeatable determination of the azimuth of the gondola relative to the sun, but has a calibration that is dependent on sun elevation and sky background. Additionally, the sensor is insensitive to rotations around the gondola-sun axis.

The rate gyros provide a three axis measurement of the motion of the the gondola, but have a drift of $8'$ hr$^{-1/2}$.

The differential GPS also provides a three axis measurement of attitude of the gondola with good accuracy, but has an rms noise of $6'$, and suffered from a severe communications problem in flight with the pointing computers in flight.

The azimuth sun sensor is calibrated by integrating the rate gyros over a series of extended ($\pm 60^\circ$) scans spaced throughout the flight at different sun elevations, and then re-registering the offset by looking at concurrent cleaned differential GPS data.

Once the azimuth sun sensor is calibrated, the telescope azimuth and elevation are determined by integrating the rate gyros with a 400s time constant. The long term average of pitch and roll is set to zero, and the azimuth is constrained on this time scale to fit the pitch and roll corrected azimuth sun sensor. Based on the gyro noise, we expect a $2.7'$ (1σ) uncertainty. Additionally, any long term pitch and roll offsets are filtered out by this procedure.

We determine the offset of each detector and the rms noise on the sky relative to the gondola attitude from sub-maps made from in-flight observations of galactic point sources. This analysis revealed an elevation offset correlated with the gondola temperature which is regressed out. The final scatter in the residual of the galactic plane point source centroids is $2.5'$ (1σ).

6. Calibration

6.1. CMB Dipole

The 90, 150, and 240 GHz bolometer signals are calibrated by their response to the CMB dipole anisotropy. The CMB dipole is an ideal calibration source for a CMB mapping receiver. Its amplitude has been measured to high precision (0.7%) by COBE/DMR (Kogut et al. (1996)). Its spectrum is identical to that of the degree-scale anisotropy and it entirely fills the BOOMERANG beams. This minimizes the final calibration error by eliminating

uncertainty in the measured spectral frequency response of each channel and in the beam pattern of the telescope.

The direction of the CMB dipole is roughly orthogonal to the BOOMERANG scan direction and it is observed continuously during the CMB scan mode. The dipole appears as a 3 mK peak-to-peak signal in the timestream, much larger than the detector noise.

The dipole signal appears at f=0.008Hz and f=0.016Hz during the 1 dps and 2 dps CMB scan modes respectively. At such low frequencies the detector signals are sensitive to 1/f noise, uncertainties in the measurement of the transfer function, and scan synchronous noise. To mitigate the worst of these while still retaining the large scale information in the dipole, the time-ordered data are high-pass filtered with a filter described by $F = 0.5\left(1 - \cos\left(\frac{\pi\nu}{f_0}\right)\right)$ for $0 < \nu < f_0$ and 1 elsewhere, where f_0 is set to 0.01 Hz.

To calibrate, we artificially sample the CMB dipole signal (Lineweaver et al. (1996)), including a correction for the Earth's velocity around the sun (Stumpff (1980)), according to the BOOMERANG scanning, and filter this fake time stream in the same way as the flight data. The 1 dps flight data are then fit to the model.

The galactic plane lies at one edge of the map, and bright galactic dust in the plane can create a spurious dipole signal. To check for Galactic contamination, various Galactic cuts are made, and the fits are expanded to include a model of dust emission (Finkbeiner et al. (1999)), filtered as above. The results are insensitive to these changes to within the quoted uncertainties, indicating that Galactic emission does not contaminate the calibration.

During the CMB scan mode, an additional scan synchronous signal from an unknown source appeared at the fundamental scan frequency. In the 150 GHz and 240 GHz channels during the 2 dps mode, this appeared as a signal larger than the signal from the dipole (Figure 18). The scan synchronous signal is well correlated with the 410 GHz channels, and a 410 GHz map is used as a template to model the noise. The fits were again extended to include the possibility of a component correlated with the 410 GHz data, and again the results do not change to within the quoted uncertainties. This indicates that the calibration is insensitive to a wide range of systematics such as atmospheric contamination, as these would be traced by the 410 GHz data.

Removal of the scan-synchronous noise limits the precision of the dipole calibration. A conservative measure of how well the scan-synchronous noise is removed is 10%, the level of agreement between the 1 dps and 2 dps calibrations.

6.2. Galactic Point Source Cross Calibration

Point source observations were made in January 2000 of the three extragalactic sources and images were made of the sources NGC3576 and RCW38 at 90 and 150GHz with the SEST telescope at LaSilla Observatory in Chile. The size of the SEST beam is 57″ FWHM at 90 GHz and 35″ FWHM at 150 GHz. The SEST data is convolved with the BOOMERANG beam to check the calibration of the the 150 and 90 GHz BOOMERANG channels. Details and source fluxes are given in Coble et al. (2002).

Maps of NGC3576 and RCW38 centered on the core of the source ($4'\times4'$ in extent) were made with 17.5″ spacing and extended maps ($10'\times10'$ in extent for NGC3576, $6'\times6'$ in extent for RCW38) were made with 35″ spacing. We use a combination of these maps for RCW38 to calculate fluxes integrated to 1 and 2 σ points of the BOOMERANG beam, and the center map only to compute the integrated flux of NGC3576. These 1 and 2 σ fluxes are dependent on beam shape, but independent of flux background.

The SEST predicted fluxes are compared with the fluxes found inside the 1 and 2 σ contours of the BOOMERANG data. These provide a cross-check on the primary BOOMERANG calibration, which is derived from the CMB dipole. We find that the 150 GHz galactic source fluxes are in agreement with the dipole calibration to roughly 6%, while the 90 GHz dipole calibration is approximately 8% higher than expected given the SEST data.

6.3. Responsivity calibration of the 410 GHz channels

Due to the higher background, the 410 GHz channels are less sensitive than the lower frequency channels. They also feature greater scan-synchronous noise. The CMB dipole, which is detected at the scan frequency, is significantly contaminated by spurious signals, and cannot be used as a calibrator. For these channels we use a different calibration method, based on the degree-scale anisotropy of the CMB, which is present in the 410 GHz maps as well as in the lower frequency maps. This is detected at a frequency much higher than the scan frequency, and a sharp high-pass filter can be used to remove scan-synchronous noise and drifts in the scan direction, while retaining the CMB signal. The pixel averaging present in the mapping process efficiently dilutes the effect of scan synchronous noise in the direction orthogonal to the scan. We use the maximum likelihood sky maps obtained with the iterative algorithm of Prunet et al. (2000). Samples of these maps have been published in de Bernardis et al. (2000).

We correlate each high-pass filtered 410 GHz map (which is a combination of noise, interstellar dust emission and CMB anisotropy) with the sum of a high-pass filtered 150

GHz map and a high-pass filtered interstellar dust template. The former is dominated by CMB anisotropy: the interstellar dust signal at 150 GHz is less than 1% of the detected mean square fluctuations (Masi et al. (2001)). The latter monitors the ISD component present in the 410 GHz map, and is obtained from the IRAS/DIRBE maps (Schlegel et al. (1998)) of interstellar dust emission. It is filtered in the same way as the BOOMERANG signals (Masi et al. (2001)). The CMB anisotropy is thus the main signal in common between the 150 GHz map and the 410 GHz map, expressed as:

$$V_{410} = A\Delta T_{150} + BI_{dust} + C \tag{1}$$

where V_{410} is the map of the 410 GHz signal to be calibrated, expressed in Volts; ΔT_{150} is the map of the 150 GHz signal, expressed in μK_{CMB}; I_{dust} is the dust template. The coefficient A can be estimated from a linear regression and is the gain calibration factor (responsivity) for the 410 GHz channel, expressed in $V\mu K_{CMB}^{-1}$. If the IRAS/DIRBE map is properly extrapolated and its brightness is expressed in μK_{CMB}, the best fit value for B is also an independent estimate of the responsivity of the 410 GHz channel.

We divide the observed sky into many $10^o \times 10^o$ patches, and for each patch where we have more than 100 pixels in common between the 3 maps we perform a best fit using Equation 1, leaving A, B and C as free parameters. We average the best fit coefficients found for each sky patch, and estimate the error in the final coefficients as the sum in quadrature of the standard deviation of the best fits plus the calibration error in the 150 GHz map.

We do not include any estimate of the systematic effects in the extrapolation of dust in the uncertainty in B. There is a galactic latitude dependance of the results for B, probably because low latitudes could be contaminated by cold dust clouds that are not accurately modelled by the IRAS/DIRBE map.

The typical total calibration error for all 410 GHz channels is $\sim 30\%$, dominated by the presence of systematic effects (the statistical uncertainty on individual fits is less than 10%).

We test the stability of the calibration over the course of the flight by dividing the data into two halves. The calibration in each of the two halves of the flight is stable to well within the total calibration error.

6.4. Calibration Stability

Drifts in the responsivity are measured by response to the calibration lamp. In every channel, the drift in responsivity is well-modeled by a linear drift that is removed from the final calibrated time stream. The average drift in responsivity over the entire 10.5 day flight

is 3.6%.

6.5. Sensitivity

The NEP of each detector is determined by dividing the voltage noise by the electrical responsivity obtained from an I vs. V load curve measured on the ground. The responsivity of the detector is scaled to flight load conditions via the bolometer DC voltage.

The sensitivity of the BOOMERANG receiver to CMB fluctuations is determined by dividing the measured voltage noise by the responsivity to the dipole. The average NEP and NET_{CMB} for each frequency is listed in Table 5.

The optical efficiency of each channel is determined by comparing the predicted responsivity to the CMB dipole to that measured in flight. The predicted responsivity of a channel is given by $\frac{dV}{dT} = \frac{dV}{dP} A\Omega \int \frac{dB_\nu(2.7K,\nu)}{dT} t(\nu) d\nu$ where $\frac{dV}{dP}$ is the electrical responsivity measured from the bolometer I-V curve, $A\Omega$ is the photometer throughput , $\frac{dB_\nu}{dT}(2.7K, \nu)$ is the spectrum of the CMB dipole, and $t(\nu)$ is the passband of the photometer channel. The average optical efficiency for each frequency is listed in Table 5.

7. Conclusion

The BOOMERANG payload performed to specification in its first long duration flight above Antarctica. The cryogenic system held the detectors below 0.285 K for the duration of the 10.5 day flight. The attitude control system and the data acquisition performed flawlessly. Ambient temperatures on the payload stayed within operating range.

The receiver performed well, achieving an average instantaneous sensitivity of 140 $\mu\mathrm{K}\sqrt{\mathrm{s}}$ in the 90 and 150 GHz single mode channels. The micromesh design for the bolometer absorbers limited the cosmic ray contamination to 5% of the data. The quasi total power radiometer provided stability over a wide enough range of signal frequencies to allow mapping of roughly 2000 square degrees of sky, a calibration to 10% from the CMB dipole, and precision measurement of CMB anisotropies on degree scales.

The cosmological results from the Antarctic flight of this instrument are reported in de Bernardis et al. (2000), Lange et al. (2001), de Bernardis et al. (2002), and Netterfield et al. (2002).

The BOOMERANG project is supported by the CIAR and NSERC in Canada; by PNRA,

Universitá "La Sapienza" and ASI in Italy; by PPARC in the UK; and by NASA, NSF, OPP, and NERSC in the US. The authors would like to thank Kathy Deniston for logistical support, and NASA's National Scientific Balloon Facility (NSBF) and the US Antarctic Program for excellent field and flight support.

REFERENCES

Bennet, C. L., et al., 1996, ApJ, 464, L1.

Bock, J. J., et al. 1996, Proc. 30th ESLAB Symp. Submillimetre and Far-Infrared Space Instrumentation, ESTEC, Noordwijk, Netherlands, ESA SP-388.

Bond, J. R., A. H. Jaffe, and L. Knox 2000, ApJ, 533, 19.

Boscaleri, A., et al. ,1990, Spie proceedings, 1304, 127.

Boscaleri, A., et al., 1990, Spie Procceedings, 1341, 58.

Boscaleri, A., et al. , 1994, Measurement Science and Technology, 5, 190.

Church, S. E., et al. 1996, Proc. 30th ESLAB Symp. Submillimetre and Far-Infrared Space Instrumentation, ESTEC, Noordwijk, Netherlands, ESA SP-388.

Coble, K., et al, 2002, ApJ, in prep.

de Bernardis, P., et al., 1993, A&A, 271, 683.

de Bernardis, P., et al., 2000, Nature 404, 955.

de Bernardis, P., et al., 2002, ApJ, 564, 2.

Finkbeiner, D. P., et al. 1999, ApJ524, 867.

Fischer M. L. , 1992, ApJ, 388, 242.

Glenn J. et al. , 2002, Applied Optics, 41, 136.

Grannan S. M. et al., 1997, Int J Infrared Milli., 18, 319.

Hivon E. et al., 2002, ApJ, 567, 2.

Hu, W., N. Sugiyama, and J. Silk 1997, Nature 386, 37.

Kogut, A., et al., 1996, ApJ, 470, 653.

Lange, A. E., et al., 1994, ApJ, 428, 384.

Lange, A.E., et al., 2001, Phys Rev D 6304, 4.

Lee, C., 1996, Proc. 30th ESLAB Symp. Submillimetre and Far-Infrared Space Instrumentation, ESTEC, Noordwijk, Netherlands, ESA SP-388.

Lineweaver, C.H., et al. 1996, ApJ, 470:38-42.

Masi, S., et al. 1998, Cryogenics, 38, 319.

Masi, S., et al. 1999, Cryogenics, 39, 217.

Masi, S., et al. 2001, ApJ, 553, L93.

Mather, J., 1984, Applied Optics, 23, 584.

Mauskopf P. D. 1996, PhD thesis, University of California, Berkeley.

Mauskopf, P. D. 2000, ApJ, 536, L59.

Mauskopf, P. D. 2001, ApJ, submitted.

Melchiorri, A. et al. 1999, ApJ, 536, L63.

Miller A.D. et al. 1999, ApJ,524, L1.

Netterfield, C.B., et al., 2002, ApJ, 571, 1.

Palumbo, P., et al., Cryogenics, 34, 1001.

Piacentini, F., et al., 2002, Astrophysical Journal Supplemental, 138 (2), 315.

Prunet, S., et al. 2000, Proc. of the conference "Energy density in the Universe" D. Langlois, R. Ansari, J. Bartlett, editors, editiones Frontieres.

Puchalla, J.L., et al. 2002, Astronomical Journal, 123(4),1978.

Rieke, F. M. et al. 1989, IEEE Trans. Nucl. Sci. 36, 946.

Romeo, G. et al., 2002, Proc of the conference "2K1BC Workshop: Experimental Cosmology at Millimetre Wavelengths" De Petris and Gervais, editors, AIP Conference Proceedings 616.

Sachs, R. K. and A. M. Wolfe 1967, ApJ147, 73.

Schlegel, D.J., et al. 1998, ApJ500, 2.

Stumpff, 1980, A&A Suppl, 41, 1.

Timusk, T. and P.L. Richards 1981, Applied Optics 20, 1355.

Welford, W.T. and Winston, R. 1989, **High collection nonimaging optics**, Academic Press, San Diego.

Yamada, Y., A. Mitsuishi, and H. Yoshinaga 1962, Journal of the Optical Society of America 52, 1.

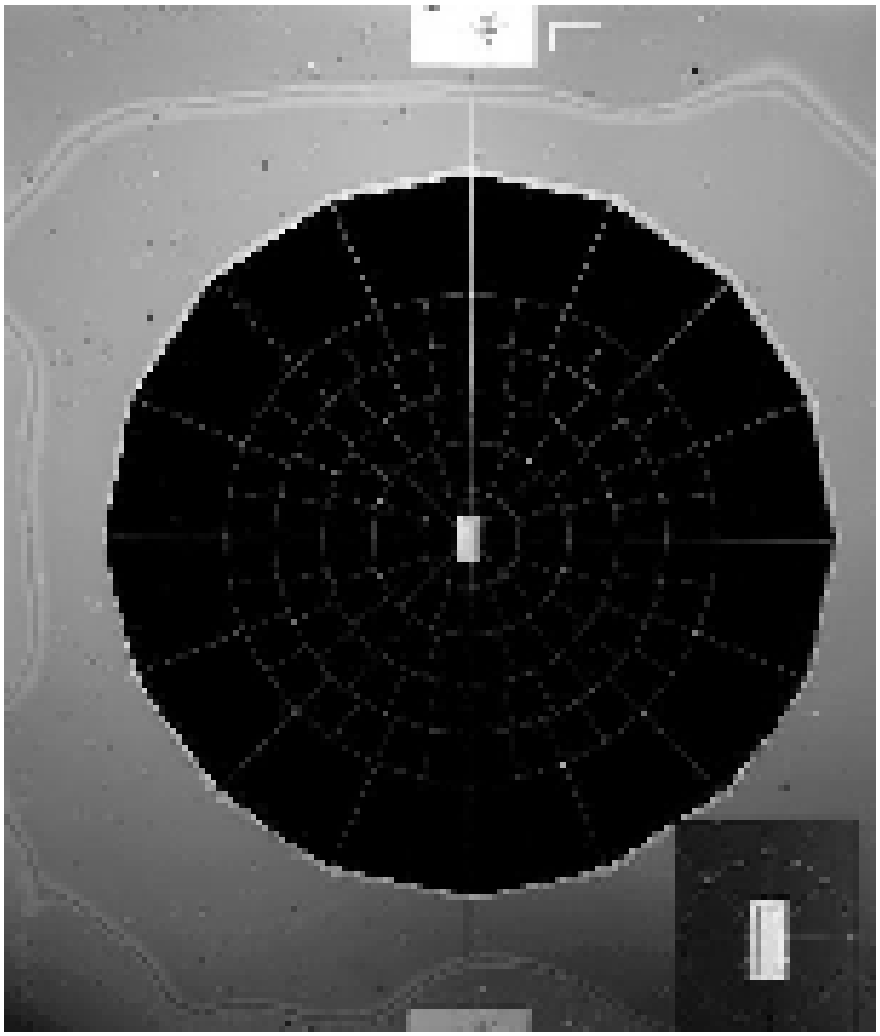

Fig. 1.— A "spider-web" bolometer used in BOOMERANG . The micromesh absorber is 4mm in diameter. The NTD-Ge thermistor is visible in the center of the micromesh absorber, and is shown in the inset.

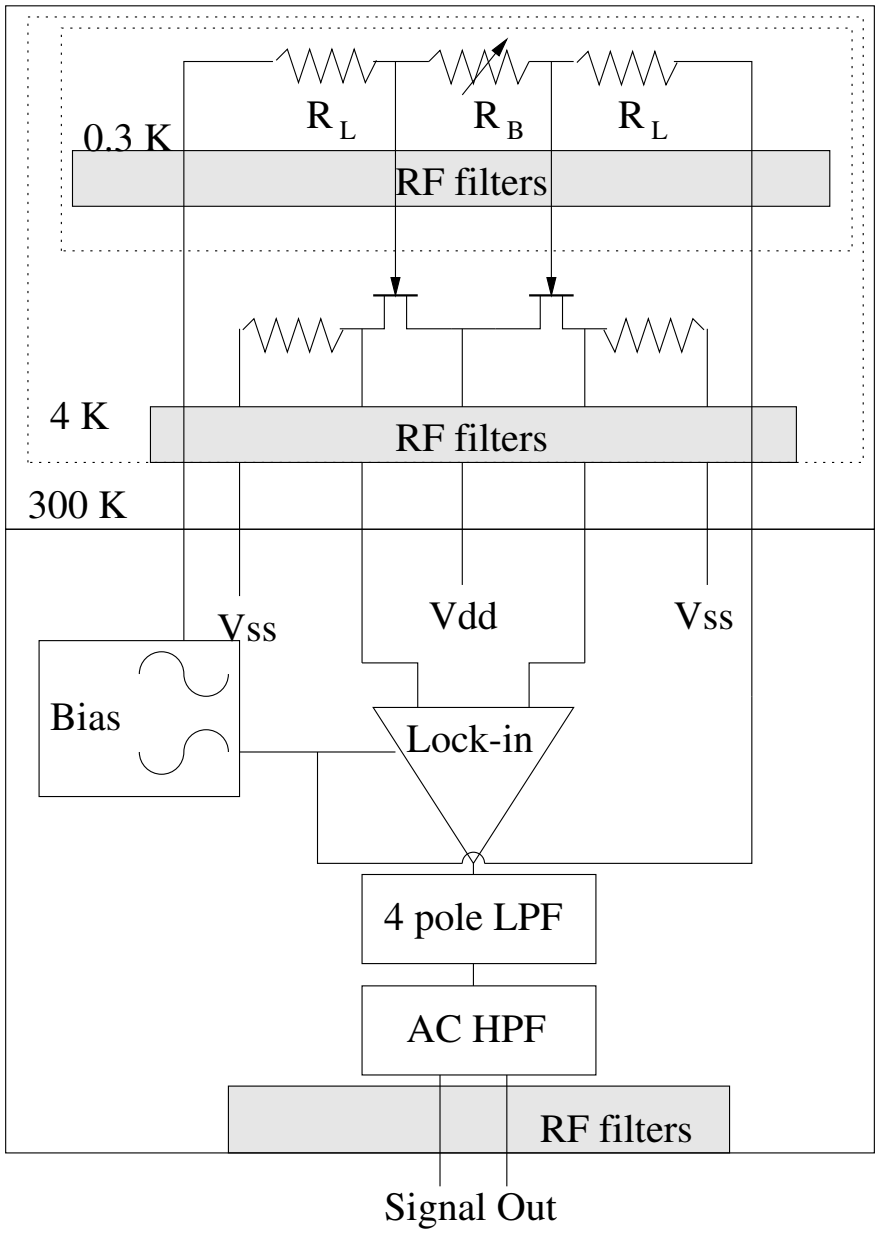

Fig. 2.— A block diagram of the bolometer readout electronics. A symmetric 331 Hz sine wave biases each bolometer across two 10 $M\Omega$ load resistors R_L. A matched dual JFET pair lowers the output impedance, and sends the detector signals to the warm electronics. There, the two signals are differenced, amplified, and synchronously demodulated. The lockin output is filtered and sent via a differential output to the data acquisition system.

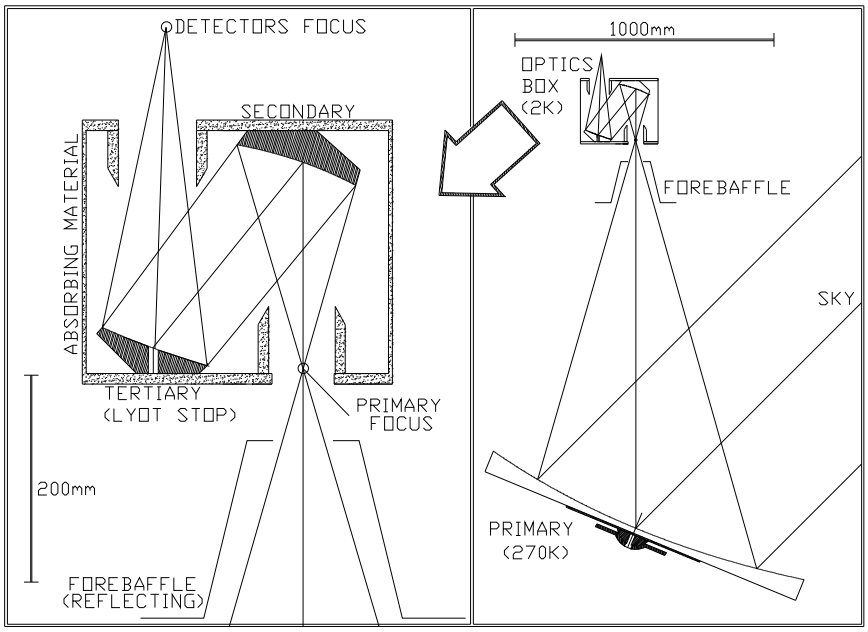

Fig. 3.— The BOOMERANG optics.

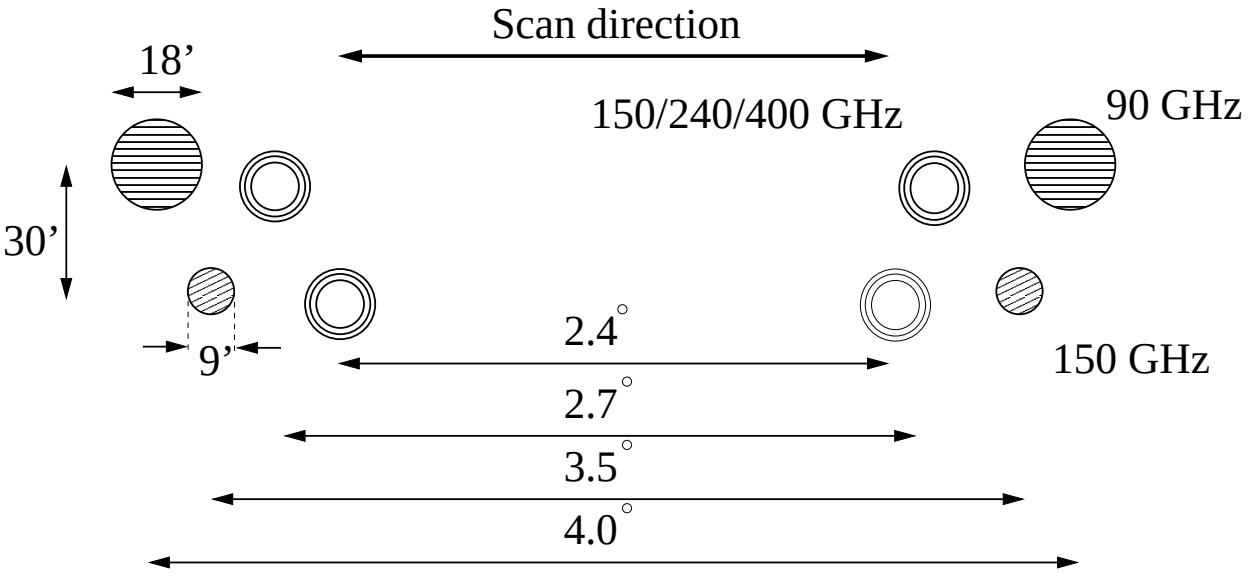

Fig. 4.— The BOOMERANG focal plane projected onto the sky. The multi-color photometer beams are roughly 9′, 14′, and 12′ for the 150,240, and 410 GHz channels respectively.

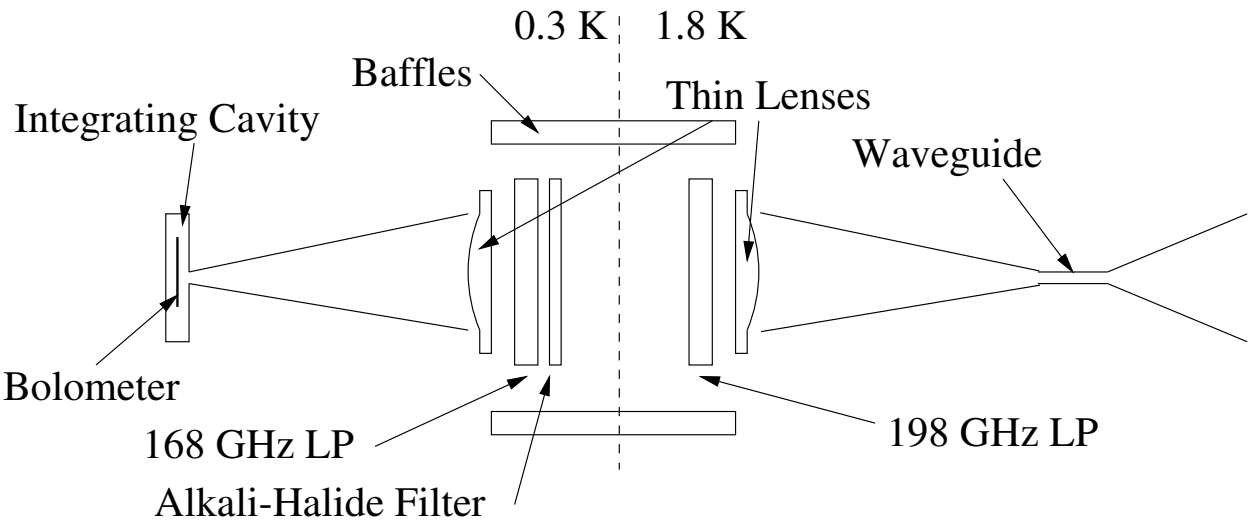

Fig. 5.— A schematic of a BOOMERANG 150 GHz single frequency feed. The 90 GHz feed structures are similar in design.

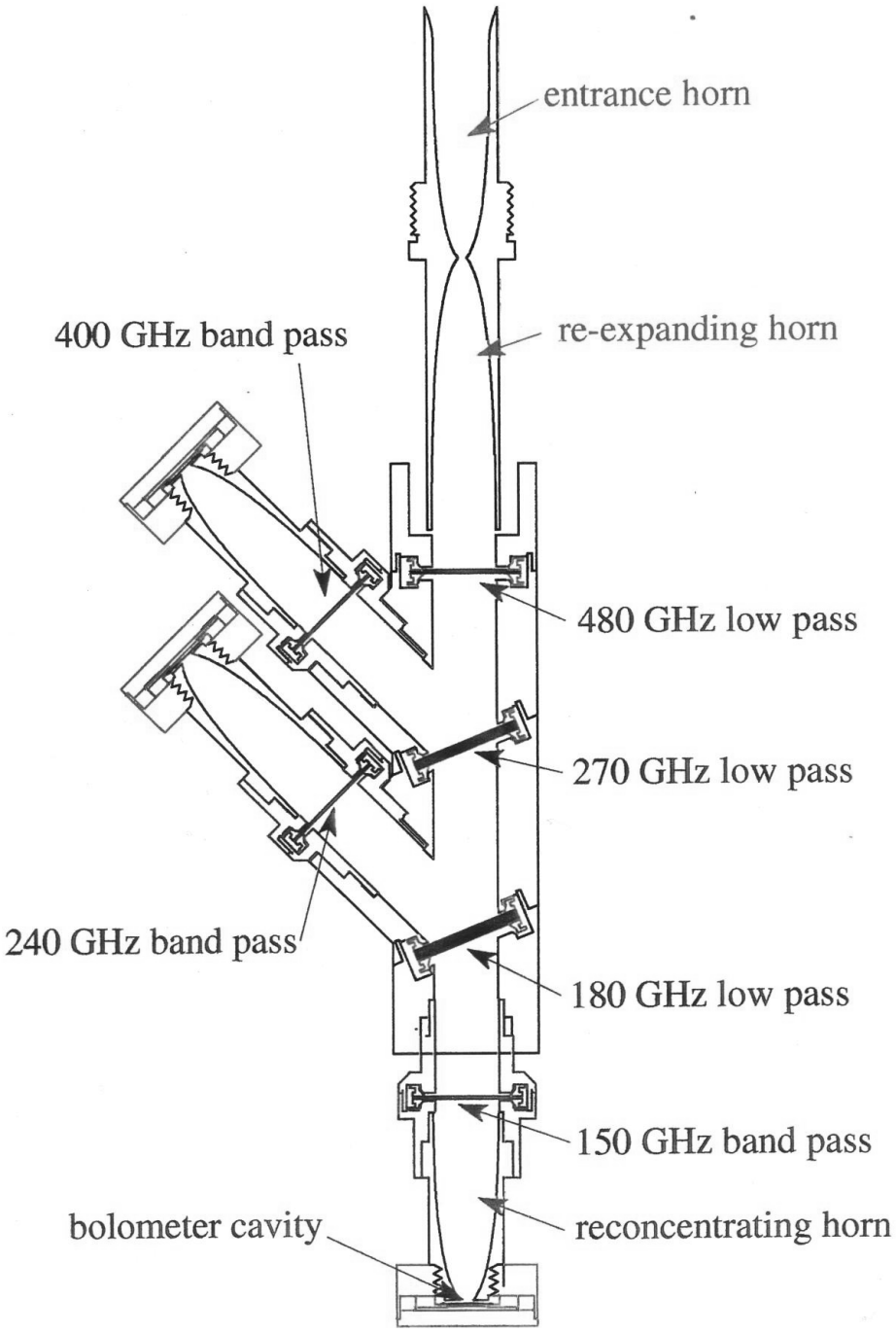

Fig. 6.— A Boomerang multi-color photometer.

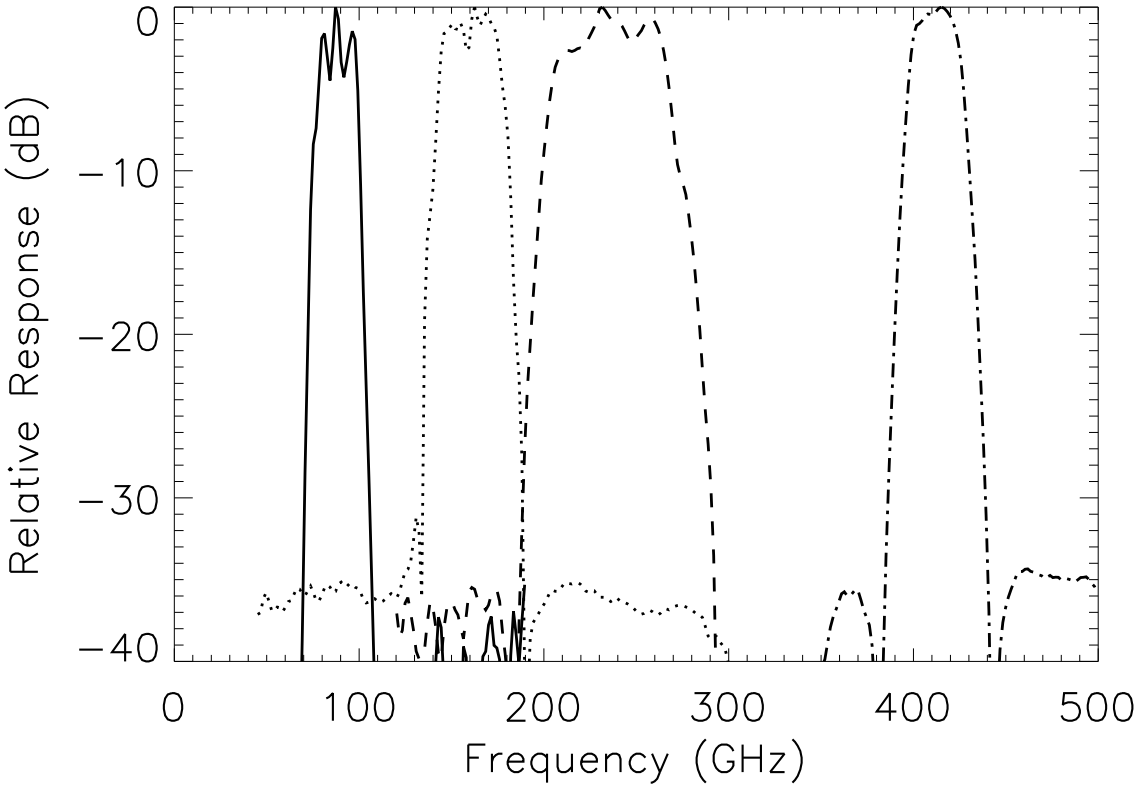

Fig. 7.— Relative spectral repsonse of four channels to a flat-spectrum source. The peak response in each band has been normalized to unity. The signal at -35 dB in each band is rectified noise.

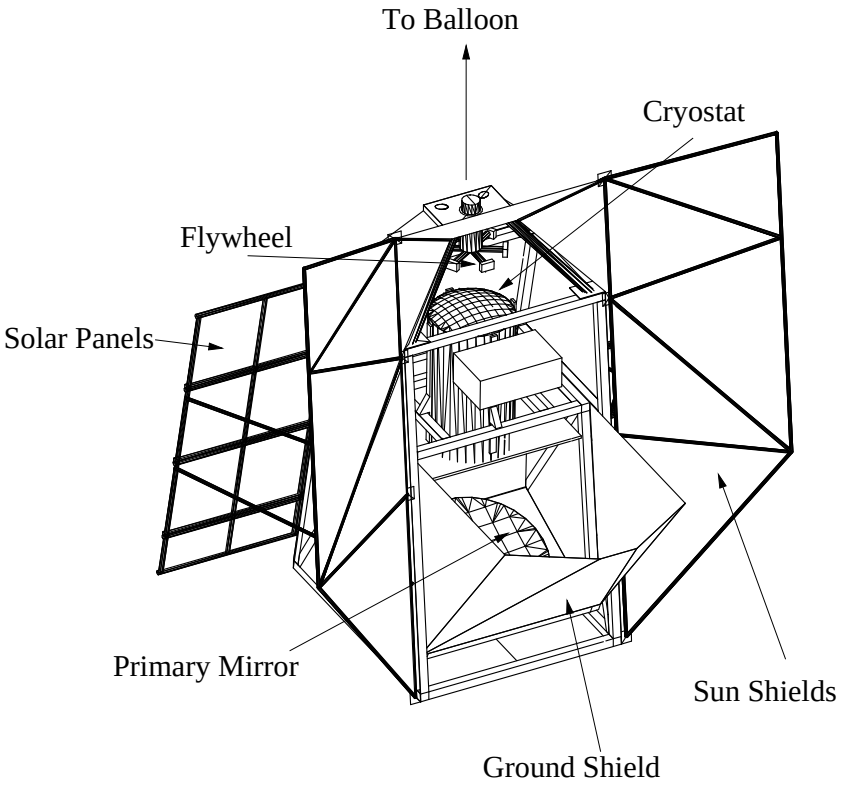

Fig. 8.— The BOOMERANG gondola. The height of the payload is roughly 4 m from the bottom to the heighest point on the sun shields. The mass of the payload at launch, including ballast, is 1600 kg. The center sun shield is oriented vertically to avoid the reflection of ground radiation to the telescope.

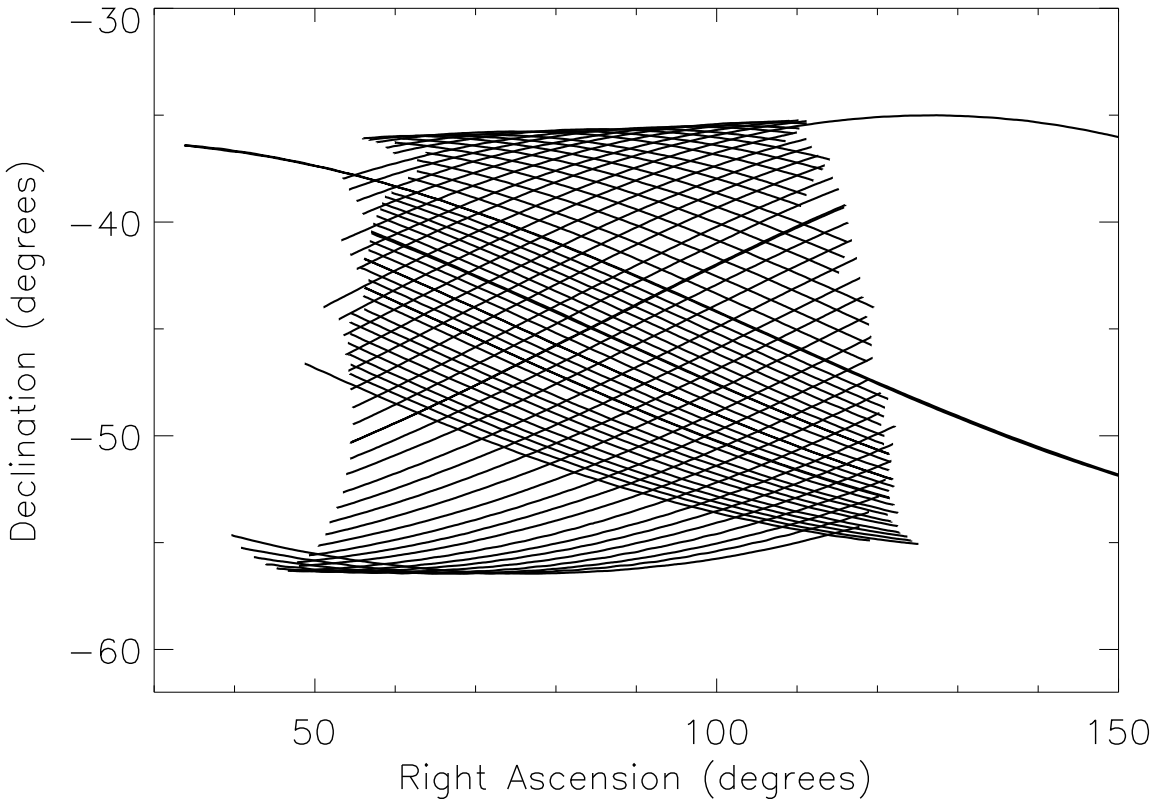

Fig. 9.— The scan crosslinking of the BOOMERANG flight. Every 20th scan from a 22.5 hour section on days 4 and 5 of the flight is shown. The telescope is at a fixed elevation of 45°. During the first five hours of this section of the data, the telescope scans at 2 dps, yielding the series of closely spaced scans at the center of the plot. During the remainder of the section, the telescope scans at 1 dps. This section of the flight is chosen for clarity; observations immediately before and after this section are made at other telescope elevations.

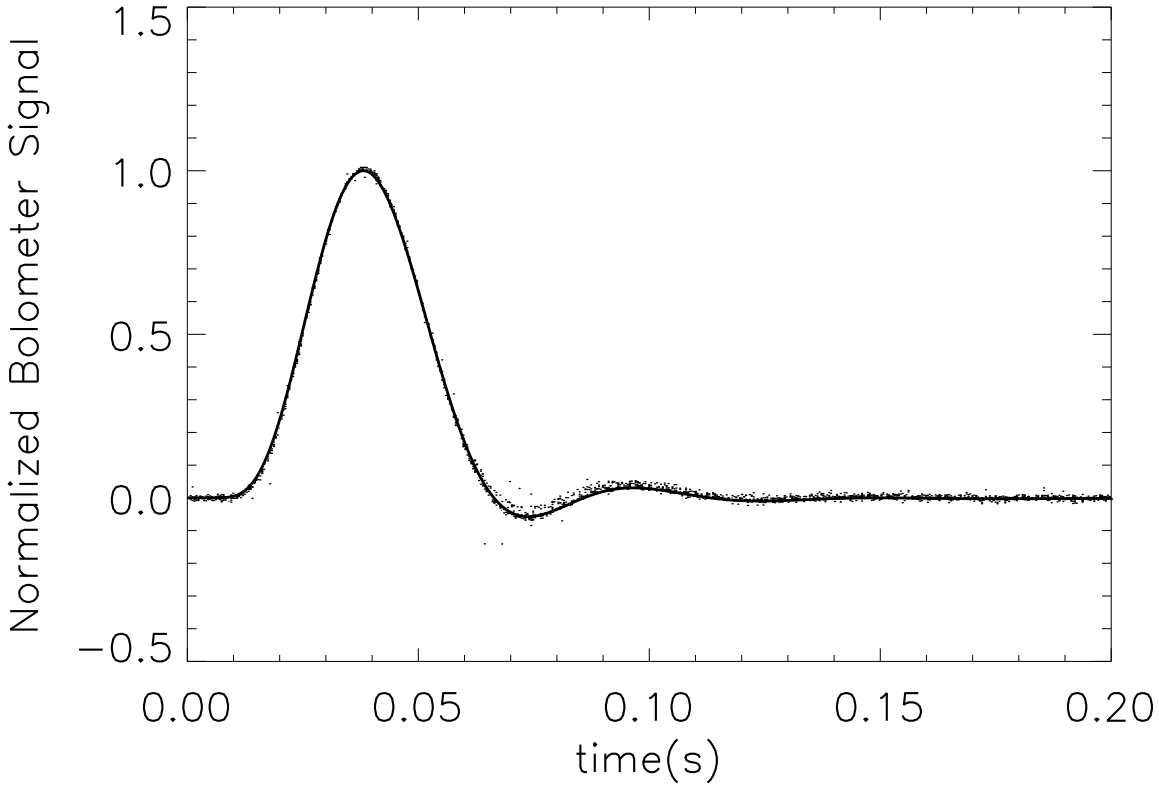

Fig. 10.— The best fit impulse response function to cosmic ray hits for one of the 150 GHz bolometers. The dots in the figure show all of the time stream data of cosmic ray hits, phase shifted to the best fit model.

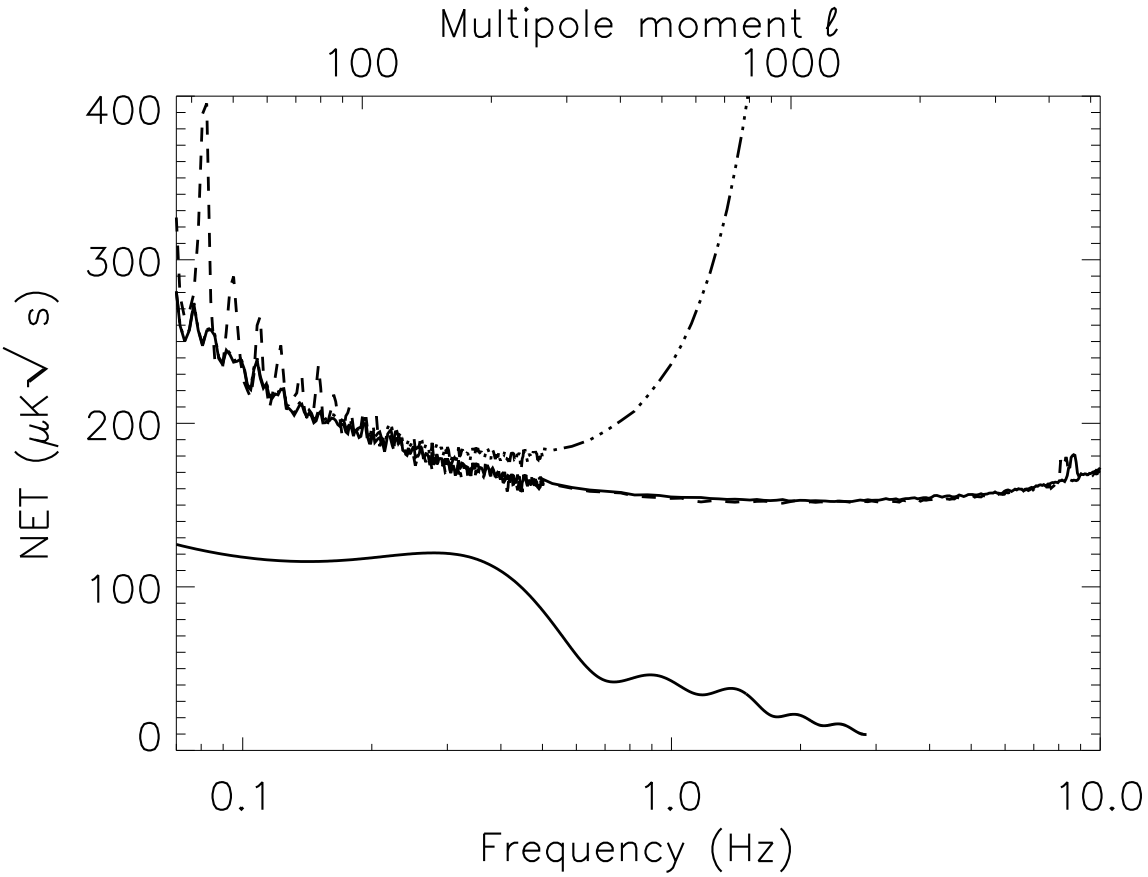

Fig. 11.— Two noise spectra of a 150 GHz BOOMERANG detector during 1 dps mode (solid line) and 2 dps mode (dashed line). The lines at $f < 0.1$ Hz are harmonics of the scan frequency. The rise in NET at high frequency is due to the bolometer's time constant $\tau = 10.8$ms. The top x-axis shows the corresponding spherical harmonic multipole for the 1 dps mode. The dot-dashed line shows the 1 dps noise spectrum convolved with the window function of a $10'$ beam. The solid line shows the expected signal due to CMB anisotropy.

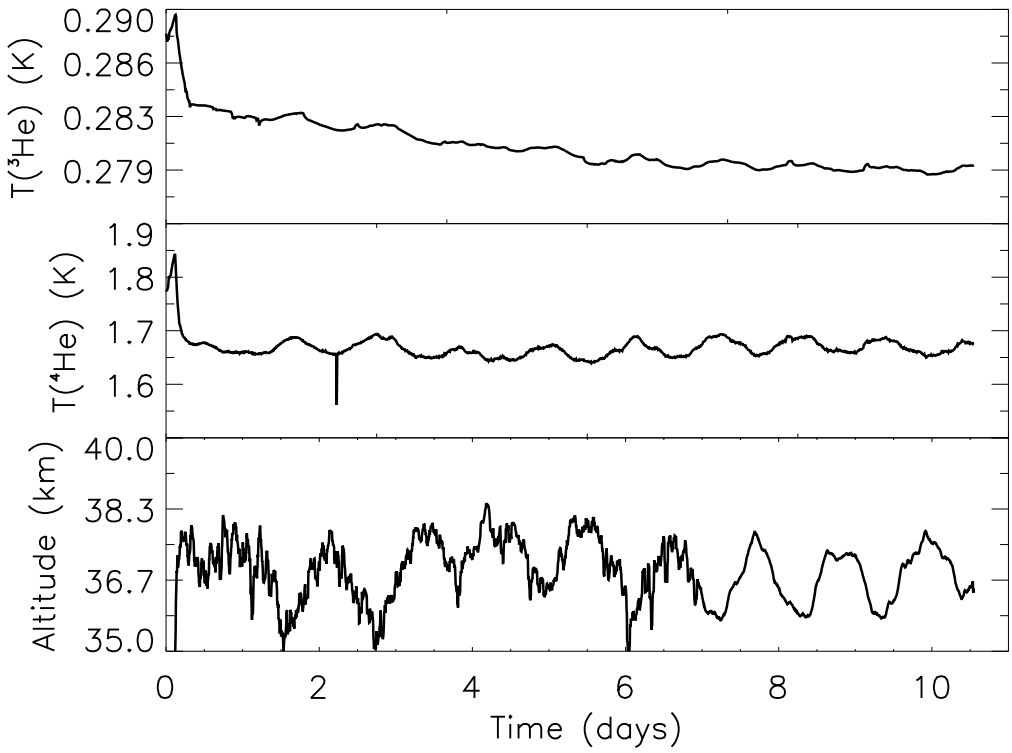

Fig. 12.— The temperature of the ^{4}He cold stage and of the ^{3}He evaporator during the flight. The lower panel shows the altitude of the payload (measured using the onboard GPS) that anticorrelates well with both cryogenic temperatures.

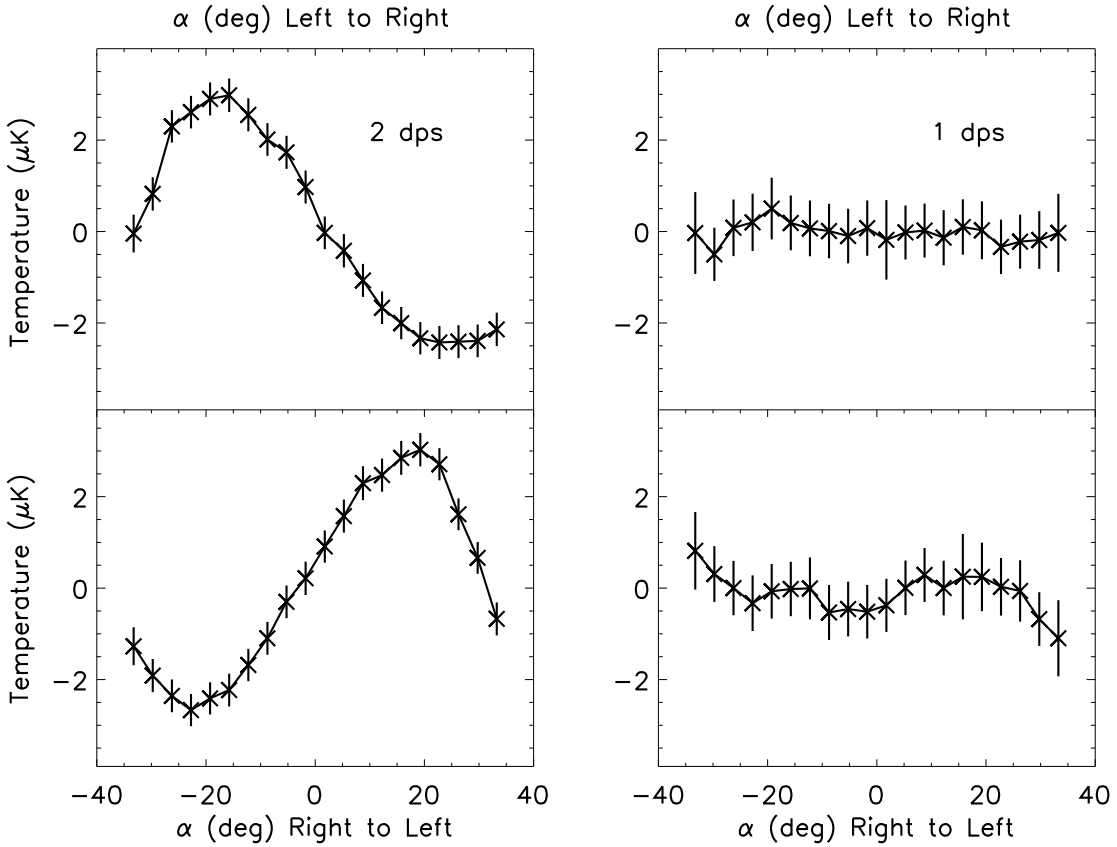

Fig. 13.— Fluctuations of the temperature of the ^{4}He cold stage, binned in angle relative to the center of the telescope scan. The top row contains data from the left-to-right direction of the scans, and the bottom row contains data from the right-to-left direction of the scans. The right column shows 1 dps data and the left column contains 2 dps data. Each plot consists of 24 hours of data.

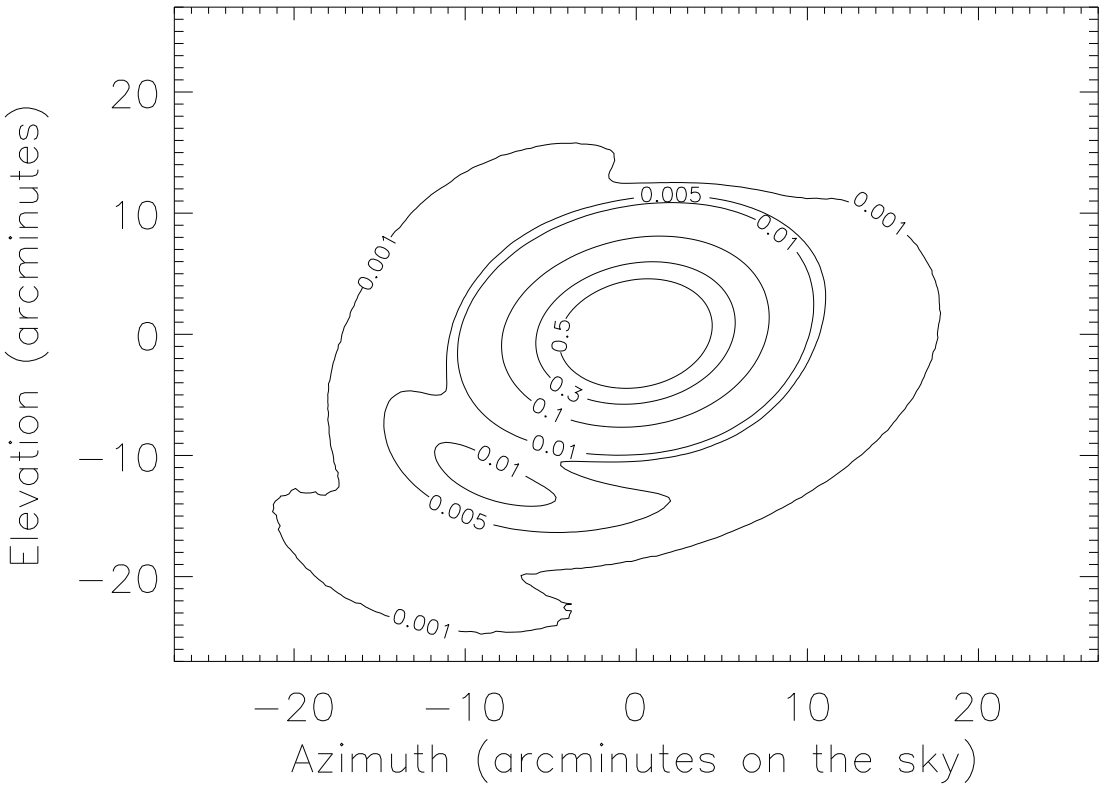

Fig. 14.— ZEMAX model for one of the 150 GHz beams, computed with a band-averaged point spread function for a gaussian illumination.

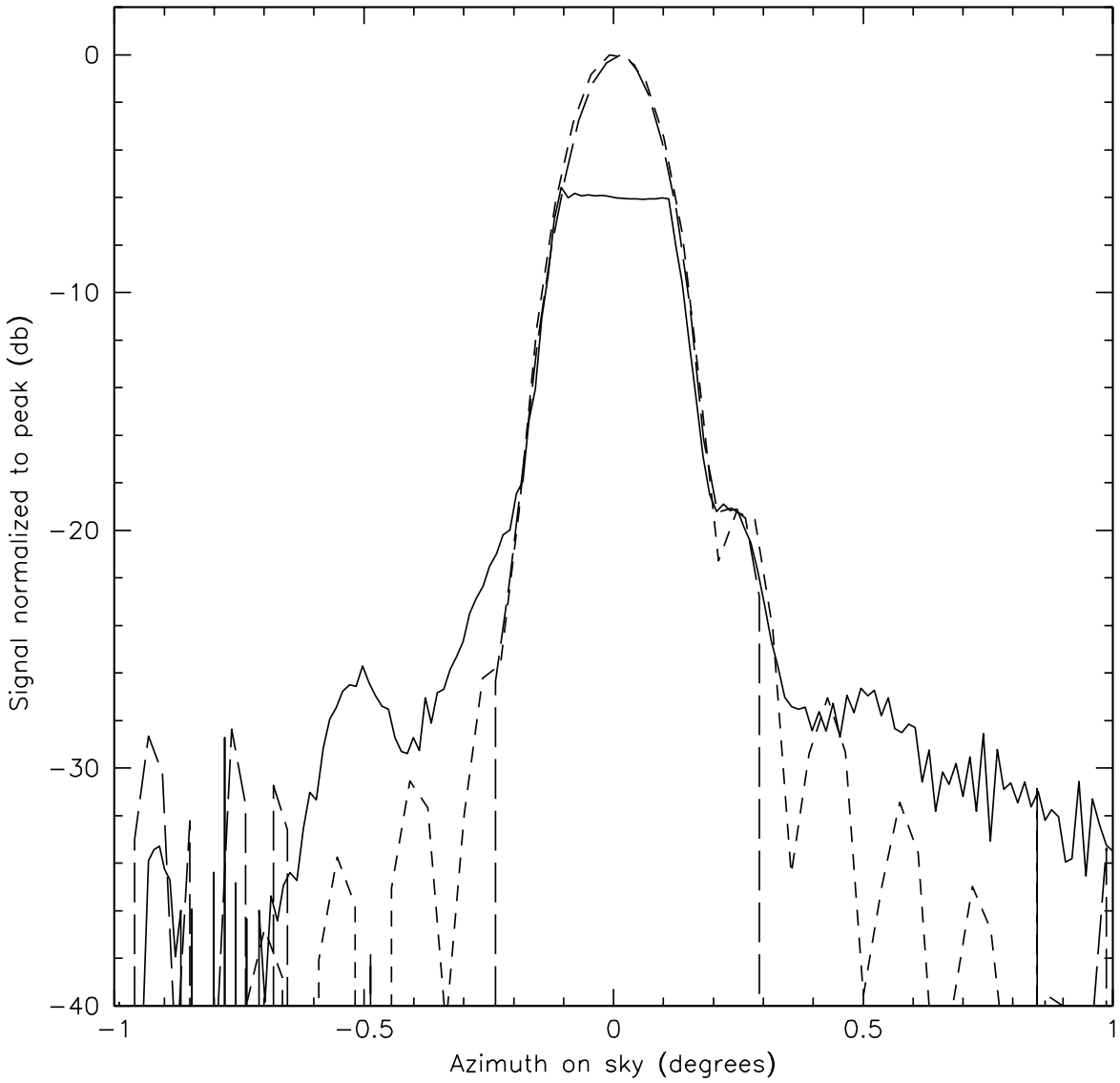

Fig. 15.— 150 GHz data from one scan in azimuth across the tethered sources. The solid line shows the signal from the large source, and is saturated in the center of the beam. The long-dashed line shows the signal from the small source. The short-dashed line shows the ZEMAX model.

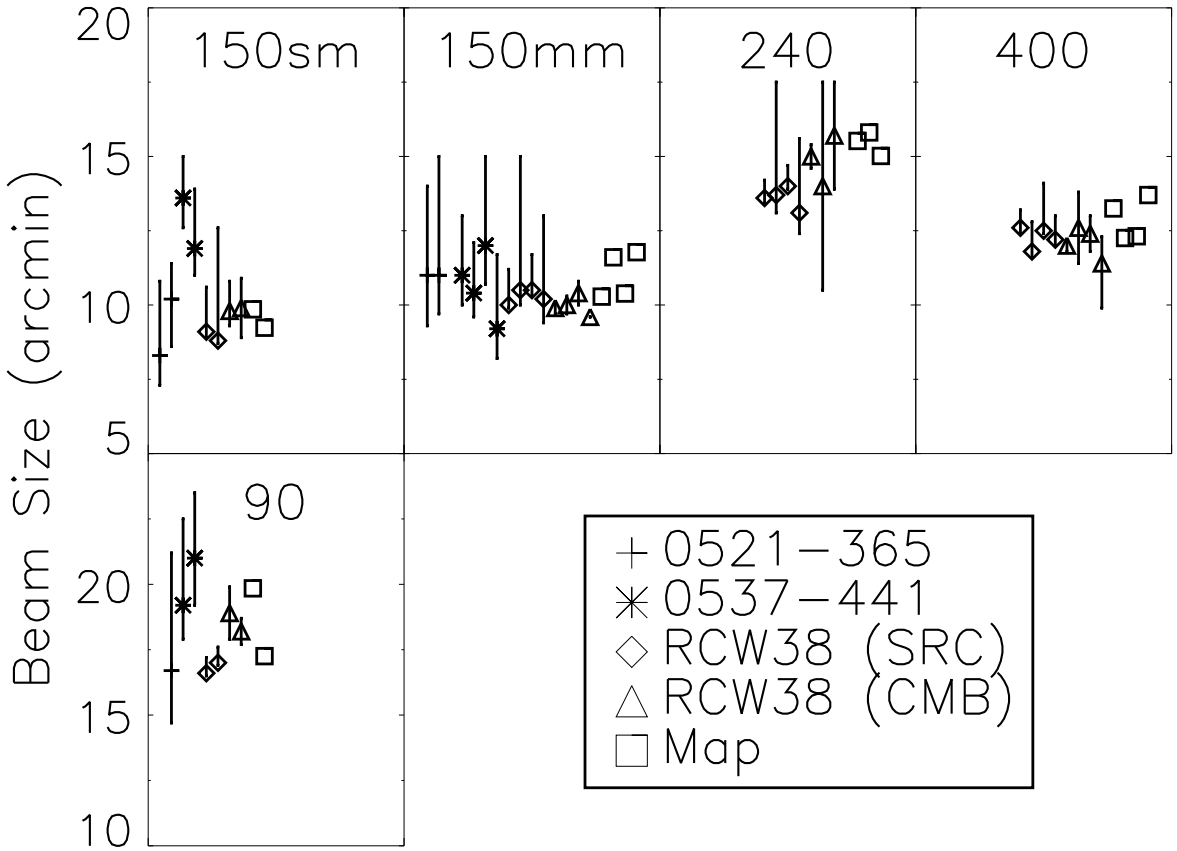

Fig. 16.— Summary of the beam FWHMs for all the channels using the three in-flight methods. "0521–365" and "0537–441" are the beam sizes derived from the radial profile of the two brightest extragalactic point sources. "RCW38 (SRC)" is the beam size derived from the targeted observation of RCW38, and "RCW38 (CMB)" is from the serendipitous observation of RCW38. "Map" is the beam size derived from the 2D binned source maps. These measurements are used only to confirm the ZEMAX+jitter model; poor signal to noise and uncertain source profiles prevent the use of the in-flight measurements for a beam map. The 150 GHz channels are divided into single-mode (150sm) and multi-mode (150mm).

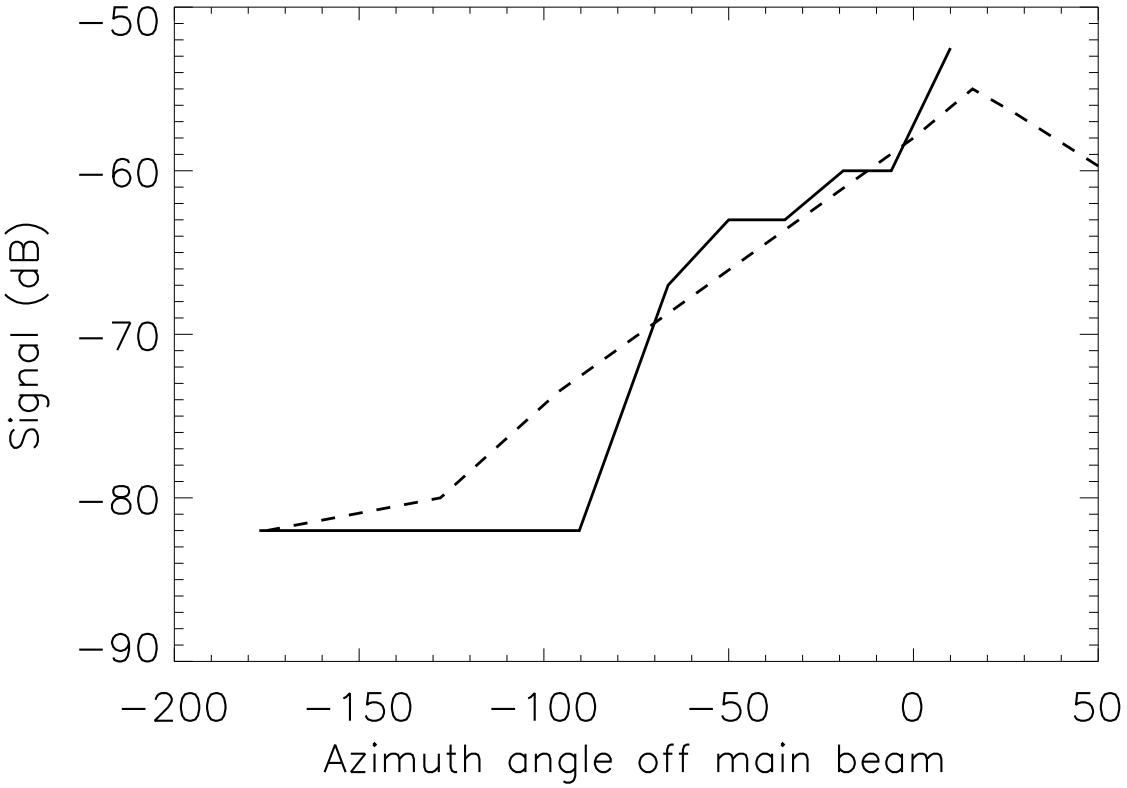

Fig. 17.— A measurement of the far sidelobes of the BOOMERANG telescope with the 150 GHz Gunn oscillator normalized to the peak on-axis response. The solid line shows the sidelobes with the source at 33° elevation and the dashed line shows the sidelobes with the source at 60° elevation. The noise floor is at -82 dB.

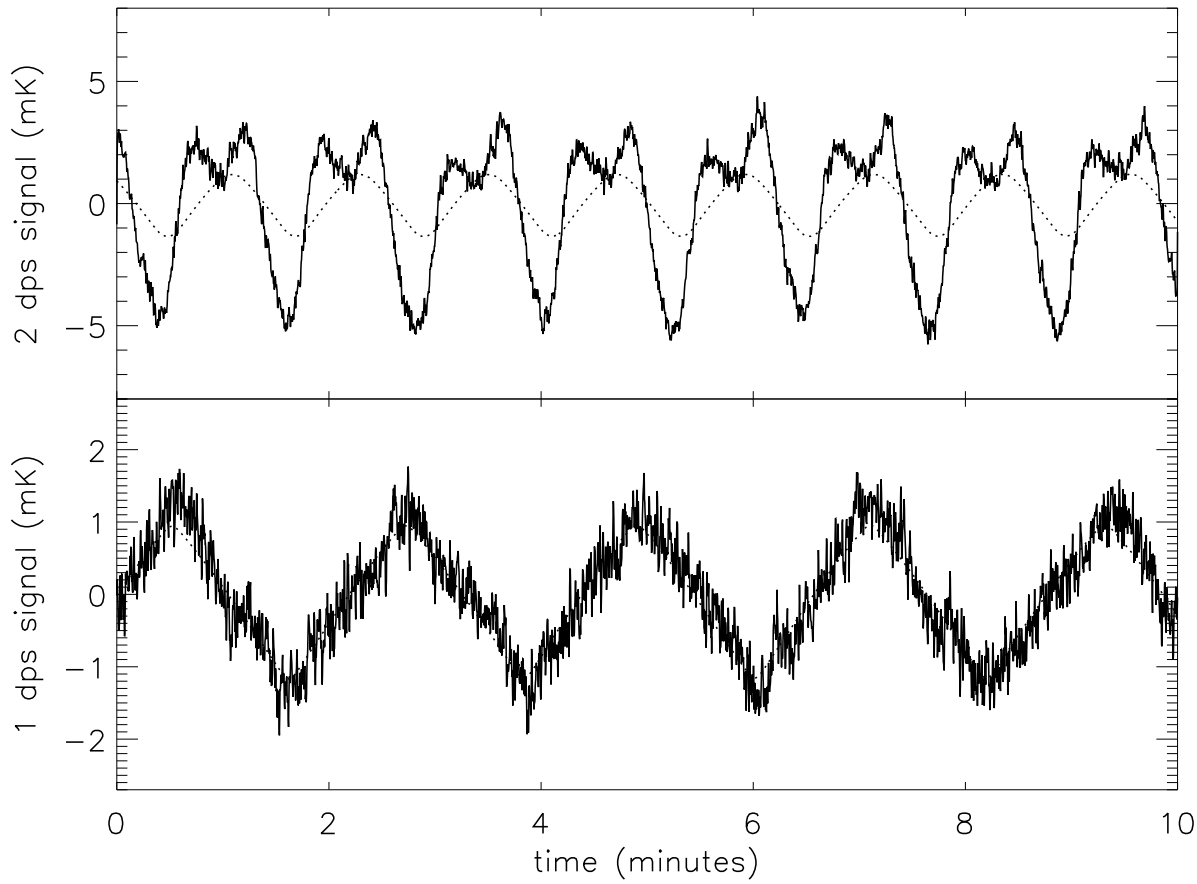

Fig. 18.— A sample section of deglitched, calibrated time ordered data for a 150 GHz detector for each of the CMB scan modes. The bandwidth has been limited to 2 Hz to show the low frequency signal. The best fit CMB dipole is overlaid in each panel as a solid grey line. In 2 dps mode, the additional scan synchronous signal dominates the dipole, whereas the 1 dps signal is dominated by the CMB dipole.

Table 1. High Frequency Spectral Leaks

ν_0 (GHz)	Thick Grill Cutoff (GHz)	Out-of-band Power (R-J)	Out-of-band Power (dust)
90	150	1.7%	23%
150 sm	230	0.5%	3.1%
150 mm	230	0.9%	5.7%
240	300	0.8%	2.6%
410	540	0.5%	0.8%

Note. — The ratio of out-of-band to in-band power for a source with a Rayleigh-Jeans spectrum (column 3) and a dust spectrum (column 4). A result much less than 100% in column 4 indicates that the dust sensitivity of that channel is given simply by the in-band dust emission. The results shown are the average over channels at each frequency. Because of different filtering schemes, the 150 GHz channels are divided into single-mode (sm) and multi-mode (mm) here. The above band leak is presumed to produce a flat response from the cutoff of the highpass filter to the cutoff of the alkali-halide filter at 1650 GHz. A single component dust model with emissivity spectral index $\alpha = 1.7$ and dust temperature $T_{dust} = 20$ K is used (Finkbeiner et al. (1999)).

Table 2. Ambient Thermal Performance

Item	Predicted Temperature (°C)	Measured Temperature (°C)
Attitude Control System	-8° to 12°	15° to 30°
Data Storage System	17° to 27°	33° to 42°
Data Acquisition System	-7° to 6°	18° to 29°
Cryostat	-29° to 27°	-5° to 13°
Bolometer Readout Electronics	-31° to 2°	21° to 27°
Solar Array	55° to 92°	57° to 68°
Ground Shield	no prediction	-37° to -17°
Primary Mirror	no prediction	-12° to 1°
Gondola Frame	no prediction	15° to 28°

Note. — A comparison of the payload thermal model with the temperature achieved in flight. The two predicted values are for the “cold” and “hot” cases. The two measured values are the minimum and maximum temperatures reached during the daily cycle. The discrepancy in predicted and in-flight temperatures for the electronics is likely due to white nylon blankets placed over the electronics to avoid excessive cooling during ascent.

Table 3. Flight Scan Modes

Target	Time (hr)
1 dps CMB	105.8
2 dps CMB	82.0
WIDESCAN	10.7
IRAS/08576	9.2
IRAS/1022	2.7
RCW38	7.4
RCW57	1.4
η Car	3.3
Cen A	2.2
A3158	9.9
A3112	3.3
A3226	6.4
Diagnostics	8.9

Note. — Time in hours spent in various scan modes during the BOOMERANG flight. The first two modes are CMB scan mode. "WIDESCAN" refers to the $\pm 60^\circ$ scans. IRAS/08576, IRAS/1022, RCW38, RCW57, and η Car refer to targeted observations of galactic sources. Cen A refers to an attempted targeted observation of an extragalactic source. A3158, A3112, and A3226 are observations of known Abell clusters. Diagnostics consists of time spent trimming the bias level and spinning the payload.

Table 4. Instrument Characteristics.

Channel	Band (GHz)	NET_{CMB} ($\mu K\sqrt{s}$)	Beam FWHM (')
B150A	148.0 - 171.4	130	9.2 ± 0.5
B150B	145.8 - 168.6	Variable	9.2 ± 0.5
B150A1	145.5 - 167.3	231	9.7 ± 0.5
B150A2	144.0 - 167.2	158	9.4 ± 0.5
B150B1	144.2 - 165.9	196	9.9 ± 0.5
B150B2	143.7 - 164.3	184	9.5 ± 0.5
90 (2 Chs)	79 - 95	140	18 ± 1
240 (3 chs)	228 - 266	200	14.1 ± 1
410 (4 chs)	400 - 419	~ 2700	12.1 ± 1

Note. — Summary of relevant instrument characteristics. Only results from the 150GHz channels are presented in this paper. B150B is not used due to non-stationary detector noise. The bandwidth limits are computed to include 68% of the total detected power for a flat spectrum source. The NET is computed at 1Hz.

Table 5. In-flight bolometer performance

ν_0 (GHz)	τ (ms)	η_{opt}	G (pW K^{-1})	R (MΩ)	NEP (1 Hz) (10^{-17} W/$\sqrt{\text{Hz}}$)	NET_{CMB} ($\mu K\sqrt{s}$)
90	22	0.30	82	5.5	3.2	140
150sm	12.1	0.16	85	5.9	4.2	140
150mm	15.7	0.10	88	5.5	4.0	190
240	8.9	0.07	190	5.7	5.7	210
410	5.7	0.07	445	5.4	12.1	2700

Note. — In-flight bolometer performance. The 150 GHz channels are divided into single mode (150sm) and multimode(150mm). The optical efficiency of the channels decreased significantly from the measured efficiency of each feed structure due to truncation by the Lyot stop. The NEP is that measured in flight, and includes contributions from detector noise, amplifier noise, and photon shot noise.